Spherical and Anisotropic Gold Nanomaterials in Plasmonic Laser Phototherapy of Cancer

Adela Ben-Yakar[1,2†], Daniel Eversole[2], and Ozgur Ekici[1]
[1]Department of Mechanical Engineering, University of Texas at Austin, Austin TX 78722
[2]Department of Biomedical Engineering, University of Texas at Austin, Austin TX 78722
[†]corresponding author: ben-yakar@mail.utexas.edu

Reference Citation:

Ben-Yakar, A., D.S. Eversole, and O. Ekici, "Spherical and Anisotropic Gold Nanoparticles in Plasmonic Laser Phototherapy of Cancer," Invited Book Chapter, Non-Magnetic Metallic Nanomaterials for Life Sciences of the 10 volume series on Nanomaterials for Life Sciences, Ed. Challa Kumar, John Wiley & Sons: Weinheim, p. 493-539 (2008).

Abstract:

Gold nanoparticles have shown great potential as *in-vivo*, optically-active, biospecific probes with highly controllable and tunable optical properties for simultaneous molecular imaging and phototherapy. The strong plasmon resonance has led to the development of a variety of nanoparticle-based cancer therapies we term Plasmonic Laser Phototherapy (PLP). Through the use of molecular specific bioagents, researchers have shown the potential for the selective treatment of cancer cells targeted with a variety of gold nanostructures. PLP has been shown through either hyperthermal therapy or localized photodisruption of cellular membranes. Both cancer therapy modes have been demonstrated across the visible and near-infrared regimes of the electromagnetic spectrum. In this chapter, we provide a review of current PLP methods. Included is a discussion of particle heating processes and we organize therapeutic results by laser pulse duration, which will affect the damage confinement during therapy.

1. Introduction:

Cancer is a major healthcare concern across the globe. United States figures alone show that slightly less than one-half of males and one-third of females will develop cancer during their lifetime, which translates to approximately 1.5 million new cases of cancer being diagnosed yearly [1]. The National Institutes of Health estimates cancer related expenditures to have cost the United States approximately $219.2 billion in 2007, spreading across the health system and other industries in part due to lost productivity [1]. These issues are of such great concern that a major goal of the National Cancer Institute is to eliminate suffering and death due to cancer by 2015 [2]. As such, there is a great need for the development of highly sensitive and cost effective technologies for the screening, diagnostic, and therapeutic treatment of cancer. The development of a multimodal tool that can combine these capabilities would be most ideal.

Nanoparticles have shown a great potential to be multimodal tools with functionality as both a contrat agent for imaging and a therapeutic agent for treatment of cancerous tissue. Several molecular imaging modalities, taking advantage of the unique optical properties of nanoparticles as contrast agents, are currently under development for cancer imaging [3,4,5,6]. While early detection can eventually reduce and even eliminate the need for expensive and time-consuming histological examinations, molecular imaging can improve the precision of cancer margin detection and the understanding of disease progression through the monitoring of biomarker overexpression. Furthermore, nanoparticles can be utilized for the simultaneous removal of cancer. The application of nanoparticle-assisted phototherapeutics includes the removal of displasia or large scale and deep tumors, and controlled therapy of cancers with minimal impact to healthy, benign tissues.

Nanomaterials have a number of advantageous characteristics in aiding the development of *in-vivo*, optically-active, biospecific probes that are highly controllable and have tunable optical properties. Among nanomaterials, noble-metal nanoparticles have shown great clinical potential in the fight against cancer due to their unique optical and chemical properties. Noble-metal nanoparticles have enhanced scattering and absorption properties in the visible to near-infrared (NIR) wavelength regimes that arise due to strong resonances upon excitation of conduction band electrons along the particle surface known as the plasmon resonance [7]. These electrodynamic properties render nanomaterials as bright contrast agents for imaging and highly effective tools for therapeutic applications. Among metal particles, gold nanostructures have

been shown to be relatively biologically compatible, showing low or negligible cellular toxicity making them ideal for *in-vivo* clinical use [8,9]. Gold nanoparticles can be synthesized relatively easily into a variety of geometries, including nanospheres [10,11], nanorods [12], nanoshells [13,14], nanocages [15], and their clusters [16,17]. Another promising particle type with strong optical properties is carbon nanostructures [18,19,20,21].

Molecular targeting of metallic nanoparticles to specific cancer biomarkers can easily be achieved through active functionalization methods. Active methods employ molecular specific bioagents such as antibodies [22] (e.g., anti-EGFR [3] and anti-HER2 [23]), DNA sequences [24], and ligands (folate [25,26]) conjugated to the particle surface for highly specific *in-vivo* delivery and binding to a disease biomarker of choice. Functionalization enables selective targeting of cells or tissues expressing their cognate receptor with high specificity [4]. For therapeutic applications, nanoparticles have also been delivered to solid tumors using passive methods that involve capping the nanoparticle with poly (ethylene) glycol (PEG) for increased biocompatibility, biostability, and retention within tissues [27,28,29].

This chapter will primarily focus on recent developments in plasmonic laser phototherapy (PLP) techniques using plasmonic gold particles as cancer therapeutic agents. For a comprehensive review of nanoparticles as imaging contrast agents for cancer diagnostics, we refer the reader to the review papers of Rebecca Richards-Kortum [30,31]. The El-Sayed group provides a nice review discussing the use of gold nanoparticles for the enhanced photothermal therapy of cancer [32,33]. In our chapter, we provide a comprehensive discussion of various PLP Techniques, extending plasmonic phototherapies beyond photothermal therapy to include cancer-killing schemes through mechanical, chemical, and plasma-mediated ablatiove effects. PLP has been divided into two distinct modes in accordance to the physical interactions between laser light and nanoparticles: continuous wave (CW) and pulsed. CW-PLP utilizes nanoparticles to initiate cell death via hyperthermic means. Pulsed-PLP localized laser damage to subcellular targets through the confinement of photodamage.

The chapter begins with a review of the plasmonic properties of noble-metal particles. The effects of size, geometry, and aggregation on the near- and far-field scattering and absorption properties are discussed. Second, the heating processes in both the particle and surrounding medium induced by nanoparticle absorption of laser energy are detailed. We begin with the elementary heating processes induced by femtosecond laser pulses and proceed to detail

how simultaneous heating and cooling occur with the application of longer pulse durations and CW irradiation. Third, the uses of nanoparticles for therapy are detailed. We begin with a discussion of single cells and tissue modifications utilizing CW laser irradiation and progress to pulsed laser irradiation where a higher precision photodisruption is possible. Cellular damage due to pulsed laser laser irradiation can be achieved through different damage mechanisms: hyperthermia, bubble formation, overlapping-bubble formation, nanoparticle fragmentation, and nonlinear absorption and plasma induced ablation processes. Finally, we summarize a number of issues that still need to be addressed before PLP techniques can fully mature and find application in a clinical setting.

2. Theoretical Understanding of Plasmonic Resonance:

Noble-metal nanoparticles have unique optical properties that arise due to the collective oscillation of conduction band electrons along the particle surface upon excitation by an electromagnetic field, which is known as the plasmon resonance [7]. This strong resonance is responsible for the enhanced scattering and absorption of light in the visible to NIR wavelength regimes that can be exploited in nanobiophotonics applications. In this section, we discuss the physical properties for the rise of the plasmon resonance. Particular insight is provided on the effect of particle size, geometry, and aggregation on the electrodynamic properties of noble-metal nanoparticles in both the far and near-fields.

2.1. Origin of Surface Plasmon Resonance:

As the size of a metallic material is reduced to the nanoscale, both the electronic properties and the optical response of the material are dramatically affected [7,34,35,36,37,38]. Changes in material electronic properties occur due to the reduction in the density of states and the spatial length scale of the electronic motion. Energy eigenstates need now to be determined by the material-substrate boundaries, making surface effects of high importance. Optically, as the size is reduced, the electrodynamic properties become size dependent and colors not typically associated with the original bulk material can be scattered. This optical phenomenon is eloquently demonstrated by observing stained glass windows as sunlight passes through. Metallic gold nanocrystals embedded in the glass are responsible for the brilliant reds found due to their interaction with the incident light. Simply by adjusting the size of a gold nanoparticle and

the environment in which it is found, it is possible to scatter light at a variety of colors ranging from deep violet to red [39,40,41].

When an electromagnetic field is incident an arbitrarily shaped noble-metal nanoparticle, the oscillating electric field perturbs surface conduction electrons, as shown in Fig 1a. Conduction electrons oscillate coherently with respect to the electric field direction, a phenomenon known as surface plasmon oscillation [42]. The ability to induce these coherent oscillations allows noble-metal nanoparticles of a certain size range to strongly absorb and scatter light [7,34,35,36,37,38]. When resonant conditions are met, the nanoparticle acts as a field intensifier and its influence on the incident wave extends beyond its geometrical boundaries. As such, the effective cross sectional area of the collected light is significantly larger than the particle itself [43]. Figure 1b presents the field lines around the particle when the resonant conditions for electron oscillation are met; Fig 1c demonstrates when resonant conditions are not met. The nature at which the electrons oscillate is dependent upon the material composition, size and geometry, as well as the dielectric constant of the surrounding medium. The oscillatory behavior strongly affects particle electrodynamic properties and location and width of the plasmon bands, providing highly controllable and tunable properties.

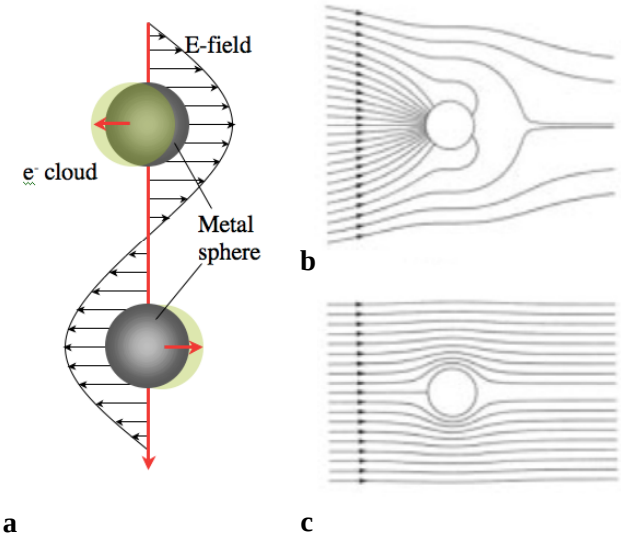

Figure 1. Description of the plasmon resonance. (a) Schematic of the coherent oscillations of the surface conduction band electrons induced by the oscillating electric field. Reproduced with permission from [42]. (b) and (c) Poynting vector field lines (excluding scattering) around a small nanosphere irradiated by laser light at the resonance and off resonance, respectively. Reproduced with permission from [7].

2.2. Description of Absorption and Scattering Properties:

For spherical, metal particles having a diameter much smaller than the incident

wavelength, the electric field intensity is uniformly distributed across the particle surface and all conduction band electrons are equally excited. In this case, electron movement can be well approximated by the Drude free-electron model, which assumes that the conduction band electrons can be treated independently from the ionic core and can move freely, whereas the ions act only as scattering centers [44,45,46]. As such, conduction band electrons have a higher polarizability and the incident electric field induces a polarization of the electrons with respect to the heavier ionic core. A net charge difference is only felt at the surface of the nanoparticle, creating a restoring force that causes the electron cloud to oscillate in phase in a dipolar fashion. In this model, retardation effects that lead to plasmon damping are negligible and the optical cross-section is dominated by dipole absorption, which can simply be described by [47]:

$$\sigma_{abs}(\omega) = 9\frac{\omega}{c}\varepsilon_m^{3/2}V_0\frac{\varepsilon_2(\omega)}{\left[\varepsilon_1(\omega)+2\varepsilon_m\right]^2+\varepsilon_2(\omega)^2}, \qquad [1]$$

where $V_0 = (4\pi/3)a^3$ is the spherical particle volume, ω is the angular frequency of the excitation radiation, and ε_m and $\varepsilon(\omega) = \varepsilon_1(\omega) + i\varepsilon_2(\omega)$ donate the bulk dielectric functions of the surrounding material and of the particle material, respectively. The absorption resonance is dependent upon the bulk material properties and the position and shape of the resonance are governed solely by the dielectric functions. From Eqn. 1, we can deduce that a strong, yet narrow absorption resonance appears at $\varepsilon_1(\omega) = -2\varepsilon_m$ if $\varepsilon_2(\omega)$ is small and does not vary much in the vicinity of the resonance.

In its basic expression, the Drude model does not predict that the absorption bandwidth is affected by particle size. Experimentally, colloidal systems having a weak cluster-matrix interaction show a well-established inverse correlation with respect to the plasmon bandwidth with particle size. To describe the bandwidth dependency on particle size, Hovel *et al.* [47] proposed a classical view of free-electron metals; here the scattering of electrons with other electrons, phonons, lattice defects, and impurities leads to damping of the Mie resonance. Briefly, in realistic metals, the dielectric function is composed of contributions from both interband transitions and the free-electron portion [48]. The free-electron dielectric function can be modified by the Drude Model to account for this dependency, giving [47,49,50]

$$\varepsilon(\omega) = 1 - \frac{\omega_p^2}{\omega^2 + i\gamma\omega}, \qquad [2]$$

where $\omega_p = Ne^2/\varepsilon_0 m_{eff}$ is the plasma frequency and the Drude γ is the size dependent phenomenological damping constant. As the particle size approaches the dimensions of the mean free path of electron scattering, the dimensions of the particle physically limit electron movement, leading to enhanced electron-surface scattering. In gold and silver, the electron mean free path is on the order of 40-50 nm [51]. Additional collision processes result in a reduced electron mean free path and increased damping. Because size effects are a function of the particle dielectric function, they are labeled intrinsic size effects [47].

As the particle size approaches the incident wavelength, scattering becomes a major contributor. Absorption effects are significantly minimized because the gold dielectric function reduces with longer wavelengths due to decreased *d*-level to *sp*-band electronic transitions. The optical response of the particle is now the superposition of both the absorption and scattering modes. Higher-order multipolar electrodynamic effects become more dominant as surface plasmons are unevenly distributed around the particle. As particle size increases, the incident electric field can no longer homogeneously polarize the surface conduction electrons and retardation effects lead to higher order modes being excited [35]. Figure 2 shows how the plasmon response changes (red-shifts and broadens) with respect to particle size.

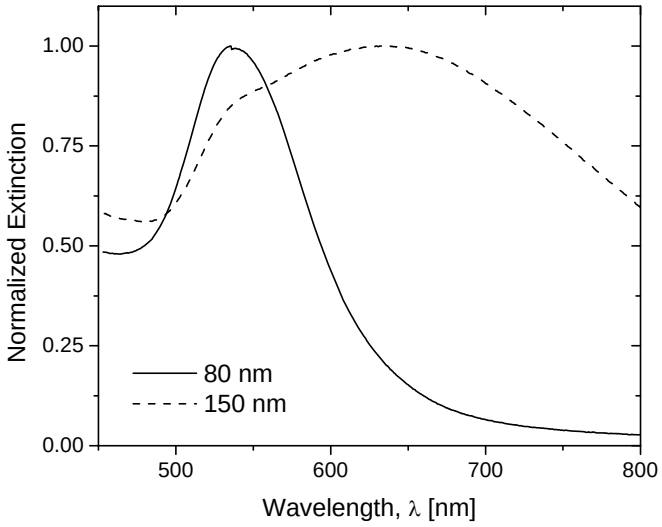

Figure 2. Size dependency on extinction spectra for spherical gold nanoparticles. With increasing particle size, the dipolar plasmon peak red-shifts and broadens. The formation of a quadrapole at the original plasmon peak is found for the 150 nm particle size.

2.3. Near-Field Scattering Dynamics

Many common applications and experimental conditions rely on light scattering measurements made in the far field, a distance far away from the particle surface. In recent years, a number of groups have been looking to develop biological technologies that rely on near-field effects of metallic nanostructures. The scattered wave in the far-field consists solely of the electric field components E_θ and E_ϕ. As the point of interest is moved closer to the particle surface, large local electromagnetic fields due to the addition of the radial electric field component E_R, are found. This can be verified in the known fact that for free-electron metals, the electric field must radiate normally to the surface. To describe the strength of the electromagnetic field in the near-field regime, Messinger *et al.* [43] introduced the following term:

$$Q_{NF}(R) = \frac{R^2}{\pi a^2} \int_0^{2\pi} \int_0^{\pi} E_S \bullet E_S^* \sin\theta d\theta d\phi \qquad [3a]$$

and

$$Q_R(R) = \frac{R^2}{\pi a^2} \int_0^{2\pi} \int_0^{\pi} E_R \bullet E_R^* \sin\theta d\theta d\phi \qquad [3b]$$

Q_{NF} represents the square of the spatially averaged electric field of the scattered wave $E_S = (E_R, E_\theta, E_\varphi)$ as a function R. The scattered field consists of all three components of the electric field vector, where the angular components, E_θ and E_φ, are perpendicular to the particle surface and the radial component, E_R, lies normal to the surface. It provides a measure for the ability of the sphere to convert the incident electric field intensity to a near-field intensity. Q_R is the main contribution of Q_{NF}, approximately 67%, which is due to the radial field component only and provides a measure of the sphere's ability to convert the incident electric field into a radially directed field. Because the E_R field component increases proportionally to R^{-2}, Q_{NF} will increase fast than Q_{sca}, which is only proportional to R^{-1}. As $R >> a$, Q_{NF} will approach the asymptotic value of Q_{sca}.

For the fundamental spherical particle geometry, with increasing particle size, the near-field scattering band red-shifts while its magnitude decreases and width broadens. Figure 3a summarizes the calculations of Q_{NF} using Eqn. 3a for varying particle diameters in an air medium irradiated with 780 nm wavelength laser light. The red-shift of the near-field scattering

is apparent, with it peaking for particles of 150–170 nm in diameter. This red-shifting phenomenon is similar to that of the absorption band, but the near-field band will red-shift faster with increased particle size. This equates to particles being able to scatter intense fields with minimal absorption. To understand this mathematically, we can observe the ratio of the near-field scattering to the absorption efficiency, $\zeta = Q_{NF}/Q_{abs}$. Figure 3b provides a plot of this ratio over a range of particle diameters. As the particle diameter increases, the degree of near-field scattering rapidly increases over the absorption at the 780 nm wavelength. When the near-field magnitude peaks at the 150 nm particle diameter, the scattering efficiency in the particle near-field is 65 times more than the absorption efficiency.

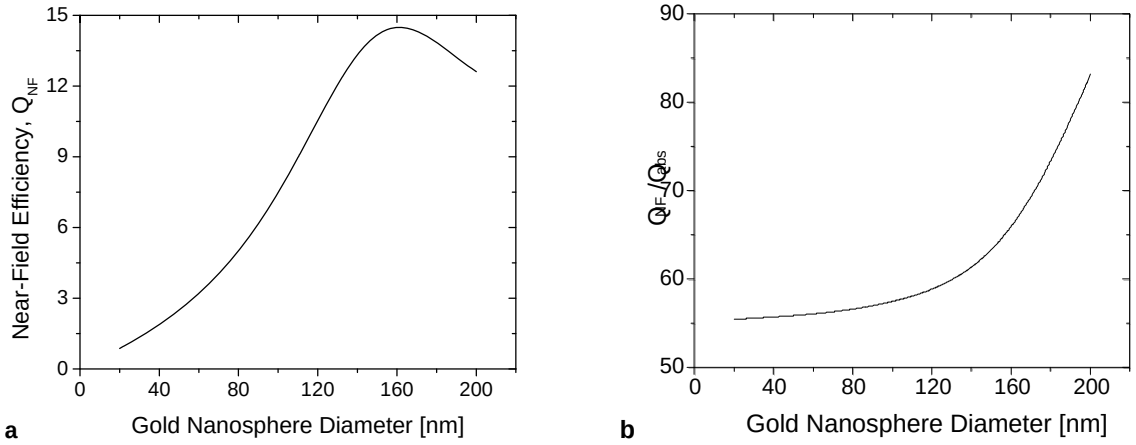

Figure 3. (a) Estimated near-field scattering efficiency, Q_{NF}, of a gold nanosphere in air as a function of particle diameter. Q_{NF} is a measurement of the particle's ability to convert incident electric field intensity into a near-field intensity. The efficiency term is estimated for an incident laser wavelength of 780 nm using Equation 13.3(a) according to [43]. (b) Q_{NF} as compared to the degree of particle absorption, , for various particle diameters.

2.4. Tunable Optical Properties of Particles:

The frequency, magnitude, and bandwidth of the plasmonic resonance and near-field properties can be tuned through particle aggregation and variation of the particle's material composition and geometry.

2.4.1. *Effect of Particle Aggregation:*

The interaction of closely spaced particles, i.e., particle coupling, has a strong effect on the location and width of the plasmon resonance. Here we will discuss coupling in two particles systems, linear chains, and in randomly oriented clusters. For a simple understanding of particle

coupling, the dipole-dipole interaction model [52] is used to describe the plasmonic interaction of two closely spaced nanospheres [53]. As was previously described, the surface plasmon response is confined along the particle surface. When certain conditions are met, the system becomes resonant and the particle strongly interacts with the incident light. Now, a second particle is placed within the oscillating field of the first particle. Upon polarization of the conduction electrons by the incident field, additional forces act upon both particles. First, let us observe a particle pair oriented such that the long axis is orthogonal to the incident electric field. In this case, the repulsive force of the surface charges is enhanced, leading to a higher resonance frequency and effectively blue shifting the plasmon resonance to lower wavelengths. The opposite effect occurs when the electric field is parallel to the long axis of the particle pair. In this case, the plasmon band shifts and stronger enhancement will be seen in the near-infrared. As a quick note, particle interaction has been seen out to separation lengths of 5 particle diameters [54].

Linear particle chains are formed with the addition of particles along the axis of interest. When unpolarized light is incident a particle chain, the plasmon band is split into two components [55]. A maximum, relating to the absorption band of individual particles, is seen at lower wavelengths, while another maximum at higher wavelengths corresponds to strong electrodynamic coupling effects by particles along the chain axis [56]. A similar effect will be discussed with nanorods later, but chains show a much more complex longitudinal resonance. Here, the longitudinal resonance depends upon the number of particles along the chain and the separation between neighboring particles. With increasing particle number and fixed particle separation, the longitudinal band red-shifts. Though, as the particle chain becomes too long, there will be saturation in the amplification of the absorption properties. Redshifting of the plasmon band and increased absorption properties are also seen when the particle number is fixed and the particle separation is reduced. For all chain sizes, as the particles get too closely spaced, the primary plasmon band begins to split into several resonances, due to increased particle coupling.

The plasmon band of randomly oriented nanoparticle aggregates follows similar trends as that of particle pairs and chains [56]. With increasing aggregate size, broadening and red-shifting of the plasmon band is observed. Additionally, the primary plasmon resonance splits into several new resonances, which is directly proportional to the number of particles in the aggregate [54].

The strength of each resonance is now dependent, though, on the size and particle orientation within the aggregate.

The near-field scattering is also greatly affected by particle aggregation [54]. With particle aggregation, the near-field enhancement becomes a function of all the individually scattered wavelets from particles in the aggregate. Essentially, primary particles in the aggregate electromagnetically couple, exhibiting additional extinction features at longer wavelengths λ, where the surface plasmon is strongly decreased in single particle irradiation. At longer wavelengths, scattering processes dominate the plasmon band, where absorption still dominates in shorter wavelengths, but will again be negligible in the NIR regime. Because the superposition of scattered waves is responsible for the near-field enhancement, aggregate size will have a finite limit, beyond which the maximal optical enhancement saturates [54,57]. This limit will depend upon particle cross-talk and deconstructive interference effects.

2.4.2. *Effect of Particle Material Composition:*

Material changes are typically the most trivial adjustment. Localized surface plasmons can arise in particles made from all noble-metal types. As such, particles can be composed of any of the noble-metals or from composites of two or more noble-metals. Composite systems include alloy and heterodyne particles [58,59].

Silver and gold are most utilized in biological applications due to their low cellular toxicity. Both metal types show a strong plasmon resonance in the visible portion of the electromagnetic spectrum. In general, the silver plasmon band is found at lower wavelengths and has a strong scattering cross-sectional area than gold. As a simple example, switching the material composition of a gold nanosphere of diameter $2a = 44$ nm to a silver particle of the same dimension affords an increase in scattering by 15 times at the plasmonic resonance [43].

In recent years, a variety of alloy and heterodyne particles have been developed. Nanocages are a gold and silver alloy nanostructure having a hollow interior and a thin, porous but robust wall [15]. By controlling the molar ratio of Ag to chloroauric acid during production, the optical response can be tuned over a broad spectral range spanning from the visible to the near-infrared. Figure 4a describes the optical response for a nanocage having a 45 nm edge length and 3.5 nm wall thickness, with a 25% residual silver alloyed with gold [60]. Additionally, noble metal coatings can be applied to dielectric particles to achieve strong

plasmonic effects. Nanoshells are a class of optically tunable, spherical nanoparticles consisting of a dielectric core surrounded by an ultrathin metal shell [14]. Through the ability to control the ratio of the shell thickness and core radius dimensions, particles can be engineered to either absorb or scatter light over a broad spectral range spanning from the visible to the near-infrared. Figure 4b shows that as the core-to-shell ratio is increased, the plasmon resonance red-shifts [61]. To adjust the core-to-shall ratio, gold shells of varying thickness were reduced onto a silica core of 60 nm radius.

2.4.3. *Effect of Particle Geometrical Changes*

Through the introduction of particle anisotropy, the plasmon band can be engineered into the NIR regime without the limitations associated with particle aggregation. Gold can be fashioned into a variety of particle geometries such as rods [62], triangles [63], and nanorice [64]. Since the rod shape has proved most important to biomedical applications, it will be the focus of the geometry discussion.

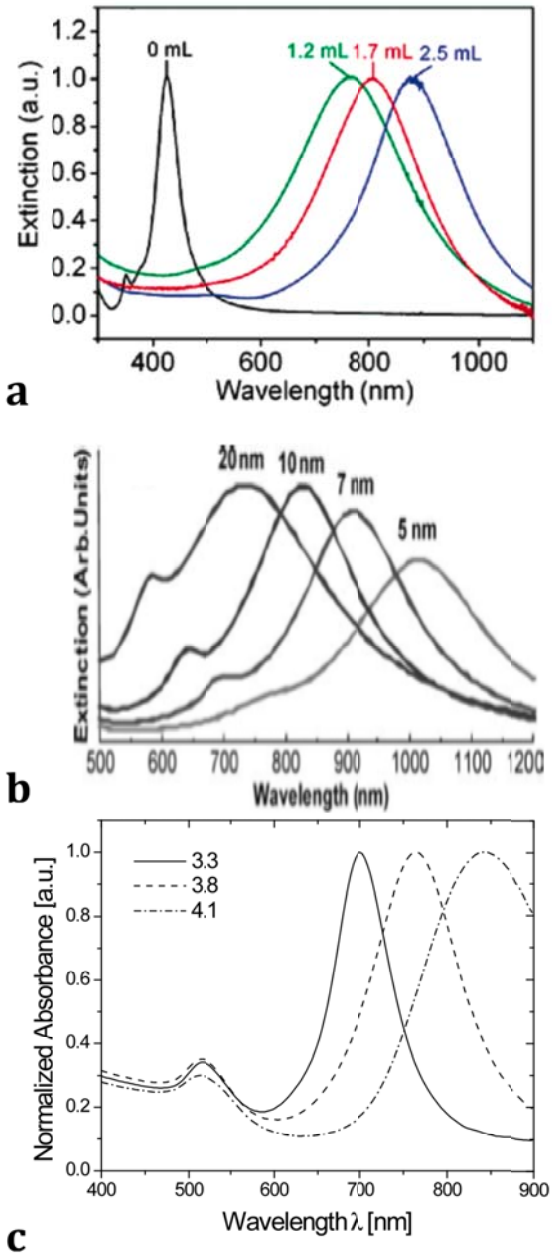

Figure 4. Evidence for the highly tunable nature of the plasmon resonance of gold nanostructures arising from variations in particle geometry and composition. (a) Nanocages, gold and silver alloy nanostructures, having 36.7 nm edge length and 3.3 nm wall thickness. Reproduced, with permission, from [60]; (b) Nanoshells, silica and gold heterodyne nanospheres, of various gold shell thickness to a constant 60 nm silica core radius. Reproduced, with permission, from [61]; (c) Gold nanorods, anisotropic nanostructures, of varying aspect ratios.

Nanorods are anisotropic structures having a longitudinal and a transverse axis that splits the plasmon resonance into two bands [12]. As was observed with particle chains, a strong lower frequency plasmon band arises due to the longitudinal oscillations of electrons and a weak higher frequency plasmon band arises from the transverse electron oscillations. This leads to strong,

tunable absorption properties in both the visible and near-infrared wavelength regimes by changing the nanorod aspect ratio. For a nanorod with aspect ratio 3.3, a small absorption peak located around 520 nm wavelength corresponds to transverse plasmon mode and the larger peak at 750 corresponds to the longitudinal plasmon mode [65]. As the aspect ratio increases, the energy separation between the two bands of the plasmon resonance increases. Figure 4c, provides experimental evidence for the plasmon shift with increasing nanorod aspect ratio. Furthermore, the plasmon band in the near-infrared regime has a much tighter full width half maximum than is achievable with spherically shaped nanoparticles.

2.4.1. *Near-Field Tunability*

The near-field enhancement is also strongly affected by geometrical changes, sharp edges [66] and surface irregularities along the particle surface [67] which can dramatically increase the overall scattering. Especially large local enhancements are found at sharp edges. Through the understanding of near-field physics, it is feasible to generate large near-field scattering enhancements at wavelengths far from the absorption resonance. Nonfundamental particle geometries can enhance the near-field scattering. For example, Krug II *et al.* [68] showed that right trigonal pyramids composed of gold and having a 45° cone angle and 675 nm long conical tip illuminated by a 825 nm wavelength plane wave can theoretically generate intensity enhancements of order 7400. As particle development continues to advance, such nonfundamental shapes will be essential to nanoparticle-based techniques.

2.5. Plasmonic Summary

In summary, we have discussed the dynamics of the plasmon resonance and how it affects the electrodynamic properties of the gold nanoparticles. Nanoparticle geometry, size, and composition can be engineered to obtain a wide range of absorption and scattering resonances ranging from the visible to NIR. For spherical particles, we find that absorption dominates the dipolar resonance for smaller particle sizes, while scattering gains greater importance with increasing particle size. With increasing particle size, we find that both the absorption and scattering components of the plasmon band red-shift. However, the absorption peak stops red-shifting when it reaches the wavelength of approximately 600 nm, beyond which it drops off to negligible amounts. For scattering-based applications, this drop-off effect in the absorption is

desirable. In contrast, absorption-based applications using spherical particles require wavelengths centered in the visible wavelength range. Other particle shapes (e.g., rods) have been engineered to red-shift the absorption band into the NIR, which will have great implications in biological applications due to greater light penetration. When observing the near-field scattering of spheres, we find that there is a continued red-shifting in the scattering plasmon band deep into the NIR. Using this information, it is possible to engineer particles very specific to a desired application.

3. Understanding Nanoparticle Heating Properties:

The degree of metal nanoparticle heating during laser irradiation depends on their optical properties and the intensity of the incident laser pulse. In this section, we briefly describe the fundamentals of laser heating and cooling (through heat diffusion) of metal nanoparticles and then present theoretical models for the accurate description of these processes. Understanding the role of laser parameters in the rate of nanoparticle heating and the extent of heat diffusion to the surrounding tissue is important to fully optimize therapeutic applications of plasmonic nanoparticles.

3.1. Fundamentals of Laser Heating of Nanoparticles and their Surrounding Medium

In nanoparticle-based therapeutic applications, the degree of heat confinement within the surrounding medium is directly related to the laser pulse duration. If the pulse duration is shorter than the characteristic time scales for heat dissipation from the particle (i.e., femto- and picosecond laser pulses) heat deposition is mostly confined within the particle during the pulse duration. Due to minimal heat loss to the surrounding water, ultrafast pulses provide the most efficient method for particle heating. Conversely, during nanoparticle heating, substantial heat loss to its surrounding occurs with the application of longer pulse durations and CW irradiation. The efficiency of particle heating reduces with heat loss and a larger volume surrounding the particle is affected as a result of the larger energies required to reach the desired temperatures.

We will begin our discussion with the most elementary particle heating process initiated by ultrafast (femto- and picosecond) laser pulses. During the exposure to an ultrashort laser pulse, electrons absorb the photon energy. These highly energetic electrons initially form a nonequilibrium energy distribution which is relaxed through electron-electron scattering on the

order of 10-50 fs in metals. A negligible amount of energy exchange occurs between electrons and phonons within these time scales and the electrons persist in high energy levels. The particle temperature begins increasing as a result of electron-phonon scattering, where the thermal equilibrium is reached on the order of 10 ps between the electrons and phonons. Meanwhile, the energy exchange between the particle and its surroundings starts taking place as a result of the elevated particle temperatures. Heat transfer across the interface occurs through the coupling of particle phonons with the phonons of the surroundings. Thermal resistance at the solid/liquid interface initially results in a large temperature jump across the boundary. The time scale to reach the thermal equilibrium across the interface is on the order of 100 ps to 1 ns depending on the particle size and the laser pulse intensity. Figure 5 schematically summarizes the fundamental processes and time scales in ultrafast laser heating of metal nanoparticles. When exposed to longer pulses (e.g., nanosecond and CW irradiation) the particle will be in a thermal equilibrium during laser heating. In this case, there is continual competition between the particle heating rate and the heat diffusion rate to its surrounding.

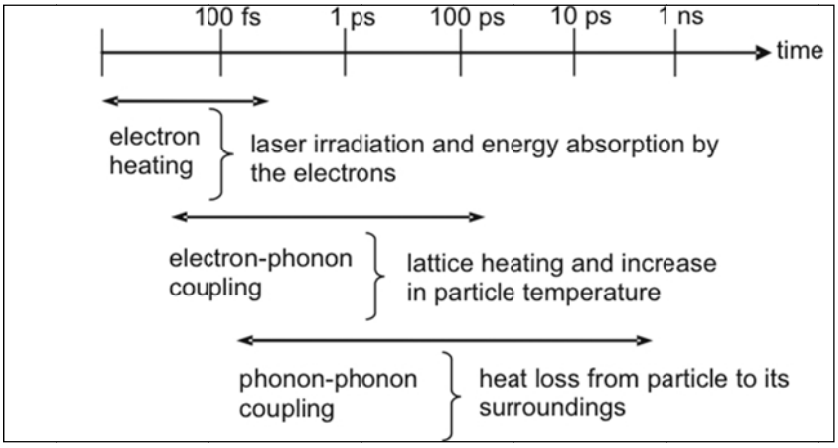

Figure 5. Time scales of the fundamental processes in ultrafast laser heating of metal nanoparticles.

3.2. Particle Heating/Cooling Models:

A variety of studies have investigated the laser-induced thermal processes occurring in colloidal systems having a weak cluster-matrix interaction. Such models are important for the understanding of heating processes in and around nanoparticles for applications such as protein inactivation and membrane disruption. Through modeling, it is possible to optimize particle size and laser duration and wavelength for the most efficient particle heating. We present a brief

overview of the developed heating/cooling models and cite a number of experimental studies supported by these theoretical models.

3.2.1. *Thermodynamic Model:*

To calculate the maximum particle temperature without temporal information, a simple thermodynamic model can be used:

$$m\int_{T_i}^{T_f} c_p dT = E_{abs} \qquad [4]$$

Here m is the mass of the particle, c_p is the specific heat, and the integration limits T_i and T_f are the initial and final temperatures of the particle, respectively. The laser pulse energy absorbed by the particle E_{abs} is directly correlated to the incident laser fluence and the effective cross-sectional area of the nanoparticle. This model is only valid when the time-scale for the heat dissipation from the particle is much larger than the heating time-scale (i.e., using ultrafast laser pulses). This simple approach assumes that all the absorbed energy is confined within the particle during the relevant time-scales of the problem. As such, the thermodynamic model gives an accurate representation of the peak particle temperature with the application of femtosecond laser pulses. For example, the Hartland group [69,70] studied symmetric breathing modes in spherical gold particles exposed to femtosecond laser pulses. They calculated breathing periods using the thermodynamic model to estimate particle temperature after irradiation. Reasonable agreement between the measured and calculated periods below the melting point was found.

3.2.2. *Heat Transfer Model:*

A more complete approach, valid for heating with both pulsed and CW lasers, utilizes the heat transfer equation to describe the temporal distribution of the particle temperature and its surroundings. In the absence of phase transformations, the general form of the heat transfer equation in cylindrical coordinates is:

$$\rho(r)c_p(r)\frac{\partial T(r,t)}{\partial t} = \nabla k(r)\nabla T(r,t) + \dot{E}_{abs}(r,t), \qquad [5]$$

where all variables are defined locally as a function of the radial coordinate r to distinguish the particle and its surroundings. $T(r,t)$ is the local temperature and $\dot{E}_{abs}(r,t)$ is the rate of the absorbed energy per unit particle volume which is zero for the coordinates outside of the particle. The material density ρ, specific heat c_p, and the thermal conductivity k are also defined locally to separate the particle from its surroundings. This general form of the heat transfer equation, however, needs to be modified to accommodate for the small size and short time scales involved in pulsed laser heating of nanoparticles, including the following three issues.

When heat flows across an interface between two different materials (such as gold and water), there exists a temperature jump at the interface that can be estimated through the knowledge of the thermal interface conductance, G. The standard assumption of equal temperatures at the boundary fails to hold in the time-scales of short-laser heating of particles due to relatively long phonon-phonon coupling times. For example, the need for thermal interface conductance during femtosecond laser heating of particles could be seen in the pump-probe spectroscopy study by Hu and Hartland [71]. In this study, a heat transfer model without the thermal interface conductance was implemented to examine the rate of energy dissipation from spherical gold nanoparticles to their surroundings. They measured the thermal relaxation time between the particle and it's surrounding and found that it is proportional to the square of the particle radius and is not a function of the initial particle temperature. However, the theoretical relaxation times as solved with simple heat transfer equations were found to be consistently faster than the experimentally measured ones. This discrepancy between the experimental and calculated results was attributed to the temperature boundary condition used in the heat transfer model that assumed equal temperatures at the interface.

The values of thermal interface conductance, G, were estimated through the measurement of the temperature decay at the interface. Wilson *et al.* [72] and Ge *et al.* [73] measured the laser-heated particle temperature decay through time-resolved changes in optical absorption. The experimental data are used to estimate the thermal interface conductance values of Au, Pt, and AuPd nanoparticles by solving the heat transfer equations in which the thermal conductance is a fitting parameter in the solution. In another study Plech *et al*. [74] investigated the lattice dynamics of spherical gold nanoparticles in a water medium by x-ray scattering. They estimated that the thermal interface conductance of G = 105±15 MW/m^{2}K matched well their experimental results.

Second, the initial thermal non-equilibrium between electrons and phonons during ultrafast laser heating of nanoparticles requires special attention. A two-temperature model [75] in describing the particle can be used to account for the electron-phonon relaxation time of the particle. Here the electrons and the lattice of the particle are treated separately and the coupling, i.e., the heat transfer from electrons to the lattice, is realized through the electron-lattice coupling factor g.

Finally, a uniform temperature profile across the particle can be assumed considering the characteristic length scales and the heat transfer mechanisms. In support of this assumption, a typical Biot number, $Bi = \mathrm{G} \cdot L_c / k_{\mathrm{gold}}$, for a nanosized particle can be estimated to be on the order of 10^{-3}, which means the temperature variation within the particle is negligible. The characteristic length L_c is defined as the volume of the particle divided by the surface area of the particle, k_{gold} is the thermal conductivity of bulk gold, and G is the thermal interface conductance. Typically less than 5% error is introduced by assuming a uniform temperature profile for Biot numbers less than 0.1.

By incorporating the concepts stated above, a new set of equations can be written to describe the transient temperature profiles for the particle:

$$C_e \frac{dT_e}{dt} = g(T_l - T_e) + \dot{E}_{abs} \qquad [6a]$$

$$C_l \frac{dT_l}{dt} = g(T_e - T_l) - \frac{\dot{Q}_w}{V_p} \qquad [6b]$$

Here V_p is the volume of the particle, T_e and T_l are the electron and lattice temperatures of the particle, respectively, g is the heat transfer rate from electrons to the lattice, and C_e and C_l are the heat capacities for electrons and the lattice of bulk gold, respectively.

The rate of heat loss from the particle to its surroundings, Eqn. 6b, is calculated by taking into account the interface conductance given by:

$$\dot{Q}_w = A_{surface} \cdot \mathrm{G} \cdot (T_l - T_{w,s}), \qquad [7]$$

where T_l is the particle temperature (lattice temperature), $T_{w,s}$ is the water temperature at the particle surface, and G is the thermal conductance at the particle/fluid interface.

The energy equation for the surrounding aqueous medium can be written as:

$$\rho_w c_{p,w} \frac{\partial T_w}{\partial t} = \nabla(k_w \nabla T_w), \quad [8]$$

where the subscript *w* is used to denote the parameters of the surrounding medium (e.g., water).

Figure 6 compares the theoretical transient particle temperatures determined from the three different models discussed above; (1) thermodynamic model (Eqn. 4), (2) heat transfer model without interface conductance (Eqns. 6-8 with G=0), and (3) heat transfer model with interface conductance (Eqns. 6-8). We have calculated the temperature of an 80 nm gold nanosphere over a 1 ns time duration after the application of a 250 fs laser pulse of 50 mJ/cm^2 average fluence and 780 nm wavelength. The results show that both the thermodynamic model and the heat transfer model including interface conductance give similar maximum particle temperatures, while the exclusion of the interface conductance estimates slightly smaller temperatures. The heat transfer model provides the exponential decay profile of the particle temperature during cooling.

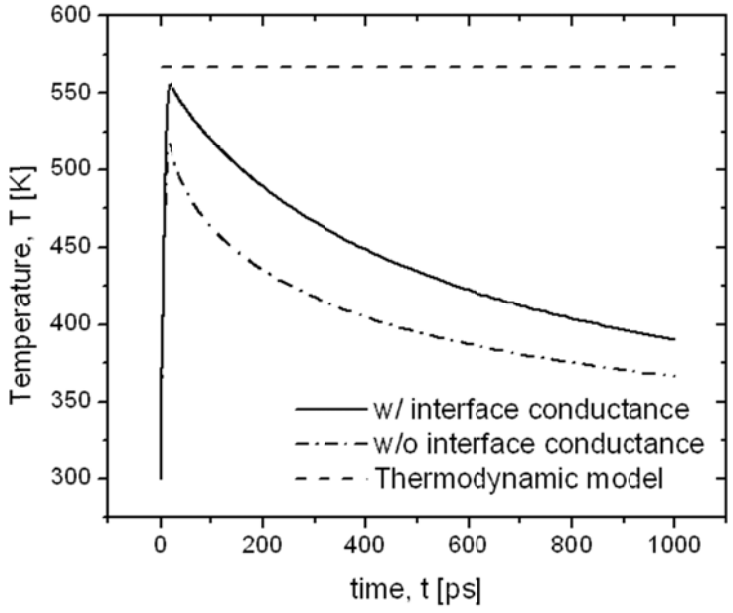

Figure 6. Transient temperature profiles of an 80 nm gold nanosphere irradiated with 250 fs laser pulse of 50 mJ/cm^2 average fluence (energy per area) and 780 nm wavelength as calculated utilizing the thermodynamic model and the heat transfer model without and with interface conductance.

To demonstrate the accuracy of this heat transfer model with thermal interface conductance, we have compared our calculations of femtosecond laser heating of gold

nanospheres [76] with the experimental results of Plech and co-workers. Plech and co-workers investigated the lattice dynamics of spherical gold nanospheres in a water medium by x-ray scattering and measured their lattice expansion [77]. Figure 7 shows the calculated values of the lattice expansion measurements of 52 nm and 94 nm gold particles at 100 ps and 1 ns after irradiation by a femtosecond laser pulse along with data provided by Plech and co-wrokers as a function of laser fluence. The model predictions are found to be in very good agreement with experimental results especially at low fluences. Beyond a certain laser fluence, the data deviates from the linear line. As also discussed in detail by Plech and co-workers, we believe that the discrepancy between predicted and measured values occurs as a result of high water temperatures at the particle surface. When the water temperature rises near the critical temperature, bubbles can form and the presented heat transfer model is no longer valid.

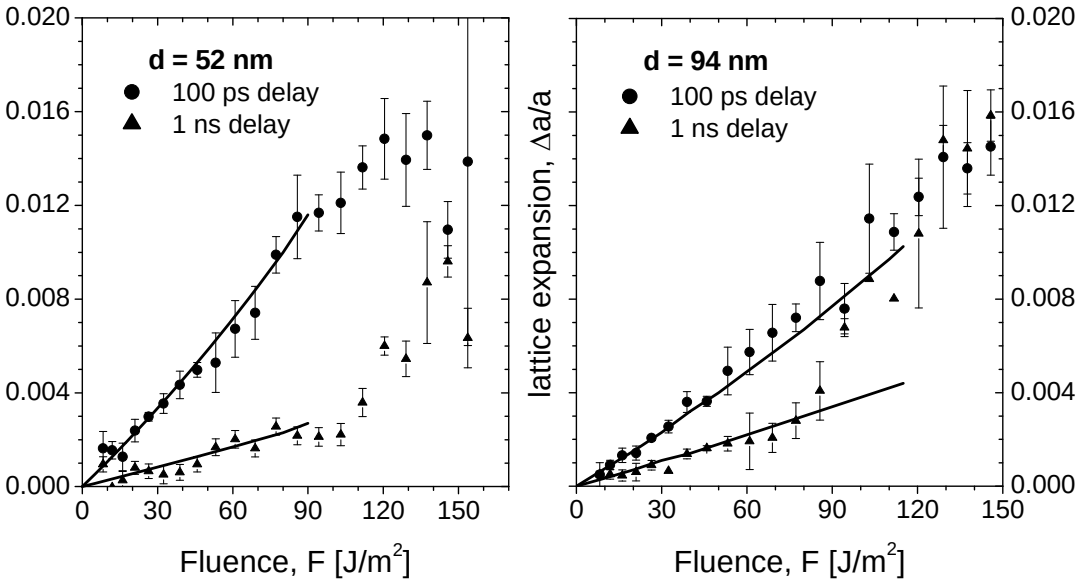

Figure 7. Validation of heat transfer model[76] with experimental data up to the fluence at which 90% critical temperature of water is reached. Lines are calculated lattice expansion of spherical gold nanospheres of 52 nm and 94 nm diameters as a function of peak laser fluence symbols are experimental data by Plech and co-workers [77].

3.3. Laser Induced Phase Changes:

As previously mentioned, the models presented above are valid in the absence of phase changes (of the particle or the surrounding medium). It is important to define the critical temperature limits to identify when the phase changes in the particle and surrounding medium occur. First, the surrounding aqueous medium has two temperature limits depending on the rate of heat transfer: a normal boiling temperature of water (T=373 K) and a critical temperature of water (T_{cr}=647 K), beyond which the water becomes thermodynamically unstable and water vapor forms. The upper temperature limit for the nanoparticle is the melting temperature (T_m=1337 K, the bulk melting value for gold).

We will first discuss the phase change of the surrounding liquid as a result of the heat transfer from laser-heated particle. A phase change induces a vapor layer around the particle which reduces the heat transfer at the surface drastically. Figure 8 presents the *P-T* diagram including the binodal (equilibrium vaporization, normal boiling) and spinodal (superheating limit) lines to illustrate the liquid-vapor phase change of water. The phase change can occur at any point between the binodal and spinodal lines depending on the rate of heating. The rate at which the laser pulse deposits energy, dictates whether the liquid temperature will heat faster than the heterogeneous nuclei will grow. Under slow heating conditions, such as is with CW or pulsed-lasers having long durations, the phase change occurs along the binodal line (for example, at T=373 K at atmospheric pressure). Slow heating will not allow extensive superheating past the binodal since excess energy will result in the growth of heterogeneous nuclei rather than further heating of the liquid [78]. On the other hand, in the case where high rates of energy (10^9 K/s) are deposited into the particle, such as is seen in short laser pulse irradiation, the surface vapor pressure built up in the surrounding fluid takes place slower compared to the temperature rise [79]. In this case, heterogeneous nuclei will not have enough time to grow and superheating can be observed [78,80,81,82]. The spinodal line forms an upper limit for the superheated liquid. When it is reached, the water becomes thermodynamically unstable and explosive phase change (homogeneous boiling) occurs. A significant amount of vapor nuclei can be found when the temperature of the liquid reaches 90% of the critical temperature at atmospheric pressure [77,80,83,84].

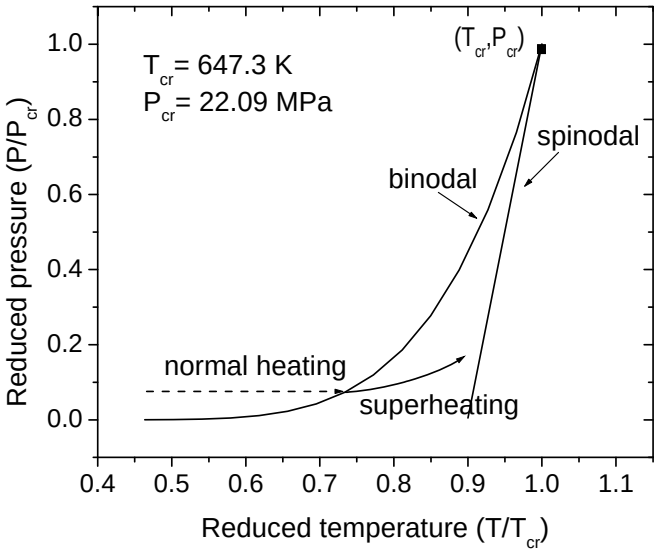

Figure 8. *P-T* diagram illustrating the liquid-vapor phase change of water.

Laser induced melting of the particle will affect the heat transfer properties of the nanoparticles as well as the laser/particle interactions during the subsequent laser irradiations. The governing equation describing the energy processes needs to incorporate changes in phase and subsequent thermophysical properties. The optical properties of particles will change due to melting and also due to the subsequent shape transformation of non-spherical particles to the thermodynamically more stable spherical particles. In addition, it has been experimentally inferred that a surface melting phenomenon can occur at temperatures much less than the bulk melting value and liquid shell nanoparticles with solid cores can be generated [69].

The shape transformation of gold nanostructures in aqueous solution from ellipsoids to spheres was investigated by Inasawa *et al.* [85]. After exposure to a 30 ps single laser pulse, the required energy for shape transformation was found to be approximately 40 fJ. This value was smaller than the calculated energy for complete melting, 67 fJ, a difference which was attributed to the surface melting phenomenon. El-Sayed and co-workers experimentally studied the melting threshold of a 44 x 11 nm nanorod by spectroscopy [86] and transmission electron microscopy (TEM) imaging [87]. A threshold energy of 65 fJ for complete nanorod melting (having 30% associated error) was found to be independent of incident wavelength [86]. In another study by the same group, Link *et al.* [87] determined a complete nanorod melting threshold fluence of

about 10 mJ/cm^2 by using femtosecond laser pulses. They also showed that laser pulse fluences lower than the threshold fluence cause partial melting of the nanorods, whereas fragmentation of the nanorods are observed at high laser fluences (~1 J/cm^2). Ekici *et al.* [76] theoretically investigated the melting fluences of nanorods 48 x 14 nm in size with respect to particle orientation to the laser polarization. We found that particles melt with 3 orders magnitude less fluence when aligned parallel to the laser polarization than perpendicular.

3.4. Summary of Heating Dynamics:

In conclusion, laser pulse duration needs strong consideration when studying particle heating dynamics. The shorter the pulse duration is, the greater the confinement of heat dissipation into the surrounding water. When the pulse duration is shorter than the electron-phonon and phonon-phonon relaxation times, as in the case of femtosecond laser pulses, it is possible to calculate the maximum particle temperature using a thermodynamic model. This approximation works quite well since heat loss from the particle is almost negligible within the duration of the pulse and the subsequent electron-phonon coupling time. Conversely, when the pulse duration is comparable to the phonon-phonon coupling times, it is no longer valid to neglect heat dissipation from the particle. In other words, the temperature estimation for relatively long pulses requires a heat transfer model for both the particle and its surroundings in order to include a descriptive picture of energy processes occurring in the system. Another difference is observed at the particle/surroundings interface where the temperature jump at the boundary becomes relatively significant as the time scale of interest gets shorter. Finally, modeling of the system with laser pulse durations longer than electron-phonon coupling times requires special attention because of the changing optical properties of the nanoparticle and its surroundings during the pulse.

In addition to pulse duration, laser induced phase changes need to be considered carefully in the studies/models of particle heating dynamics. First, the particle melting and the subsequent shape transformation could be observed at high temperatures. Second, a phase change in the surrounding medium of the particle could be observed. Either of these phase transformation changes the heat transfer properties drastically and requires more complicated models (i.e., a solution for the full set of compressible equations) to represent the effects of pressure and bubble formation around the particle.

4. Plasmonic Laser Phototherapy (PLP):

The strong plasmon resonance of noble-metal nanoparticles has led to the development of numerous nanoparticle-based laser therapeutic treatments, which we term Plasmonic Laser Phototherapy (PLP). Through the use of molecular specific bioagents such as antibodies and ligands, researchers have shown the potential for the selective treatment of cancer cells targeted with a variety of gold nanostructures. Nanoparticle-based cancer treatment has been shown through either hyperthermal therapy or localized photodisruption of cellular membranes. Both modes of cancer therapy have been demonstrated across the visible to NIR wavelengths of electromagnetic spectrum. Extended beyond cancer treatment, photoactivated nanoparticles have been used to inactivate proteins [88,89] and perturb DNA [90], and chromatin [91] through direct coupling of the nanoparticle to the desired structure. Additional therapeutic prospects exist in gene transfection [92], proteomics, angiogenesis, atherosclerosis, virology [93], and bacteriology [94].

As previously mentioned, two distinct modes for the selective killing of cancer cells are currently being investigated. The first PLP mode involves the generation of thermal damage through hyperthermia induced by the CW-laser heating of nanoparticles. Hyperthermia is defined as the heating of tissue to a temperature of 41-47 °C for tens of minutes [95]. Tumors have a reduced heat tolerance due to their inability to easily dissipate heat, which is caused by the disorganized and compact vasculature structure [32]. A fundamental aspect of photothermal therapy is that the incident light is tuned to the frequency of the nanoparticle absorption resonance, providing maximal energy absorption by the particle. Due to the strong absorption dynamics of metallic nanoparticles, large temperature rises in tissue structures can be achieved to selectively kill cancer cells with limited damage to healthy surrounding tissue [32]. Plasmonic photothermal therapy causes irreparable tissue damage through protein denaturation, coagulation, and cell membrane disorganization.

The second PLP mode involves the application of pulsed lasers to induce localized photodamage to cellular membranes in the vicinity of the nanoparticle. Depending upon laser pulse duration and fluence, a variety of photoactivated processes (i.e., photothermal and photomechanical effects/damage) including hyperthermia, bubble formation as a result of boiling or explosive boiling, and particle fragmentation can be utilized to locally disrupt a biological

membrane. It is important to remember that with decreasing laser pulse duration to the nano and sub-nanoscale, photothermal and photomechanical effects/damages in the tissue can be confined to the particle near-field as a result of greater efficiency in the heating and scattering processes. This confinement provides the possibility for membrane- and molecular-specific phototherapy with high specificity.

Nanoparticles have highly tunable plasmon resonances that allow for therapy over the entire visible to NIR wavelengths. The fundamental, spherical particle shape typically has a resonance from 400-600 nm [7]. Through the engineering of anisotropic (nanorods, nanocubes) and heterodyne (nanoshells) particles, the resonance is red-shifted into the NIR wavelengths. This tunability is important when accessing the size of the region of interest. For surface lesions or *ex-vivo* cell treatments, where light does not need to penetrate deep within tissue, visible wavelengths could be appropriate. Deep lesions require laser wavelengths not highly absorbed by water in cells and tissues. NIR wavelengths should be used for large-scale lesions and those lesions deeply embedded within a tissue structure.

In this section, we review the various approaches of nanoparticle-based laser therapeutic treatments. We commence with a discussion of CW plasmonic photothermal therapies. Single cell and large tumor manipulation are presented. We then proceed to continue with a discussion of micro- and nanoscale manipulation of subcellular materials using pulsed lasers. To introduce the concept of confinement we begin with localized photothermal therapy for the manipulation of protein expression and then discuss how laser confinement has been used in a variety of cancer treatment methods. It is our hope that after reading this section, the reader will begin to understand how particle shape and size and laser pulse duration and wavelength can be engineered to fulfill the parameters for a large set of cancer phototherapies.

4.1. Continuous Wave Laser Plasmonic Phototherapy

The first class of nanoparticle-based phototherapy applications utilizes CW-lasers. Here, the goal is to deliver a lethal dosage of heat into large-scale tumor structures in which a high density of nanoparticles are embedded while causing as little damage to intervening and surrounding normal tissue as possible. Specifically, for photothermal therapy (hyperthermia), tissue temperatures are moderately raised to 41-47°C for several minutes, which is high enough to cause cellular membrane disorganization and protein denaturation. Table 1 summarizes recent

demonstrations of plasmonic photothermal therapy of cancer cells *in-vitro* across the visible and NIR wavelength regimes utilizing gold nanospheres, nanorods, and nanoshells. We commence with a number of *in-vitro* cells studies and work towards a discussion of *in-vivo* studies where two techniques for effective delivery of particles to tumor regions are presented.

4.1.1. *In-vitro cell studies:*

Nanoshells, originally developed by the Halas group [14], are a class of optically tunable nanoparticles consisting of a dielectric core surrounded by a thin gold shell, have shown great promise for photothermal therapy applications. Through the ability to control the ratio of the shell thickness and core radius dimensions, the resonant wavelength can be tuned from 500 nm to 2 microns [61]. Specifically, gold shells of 10 nm encasing a silica core of 110 nm having a peak resonance centered at 820 nm were found to be most effective in therapy due to their high particle absorption in comparison to the tissue.

Researchers at Rice University have primarily been responsible for much of the experimental evidence for the efficacy of photothermal therapy with nanoshells. In proof-of-principle experiments they demonstrated *in-vitro* photothermal destruction of HER2-positive SKBr3 breast adenocarcinoma cells [23,96,97]. Here, cells bound with the anti-HER2 conjugated nanoshells were irradiated for 7 min with CW laser light operating at 820 nm wavelength with a total intensity of 35 W/cm^2. As shown in Fig. 9, it was determined that all labeled, malignant cells within the laser spot were photothermally damaged, while unlabeled cells remained intact[97]. Stern *et al.* [98] at The University of Texas Medical Center experimentally determined that cells need to be labeled with approximately 5000 nanoshells for the most effective photothermal treatment.

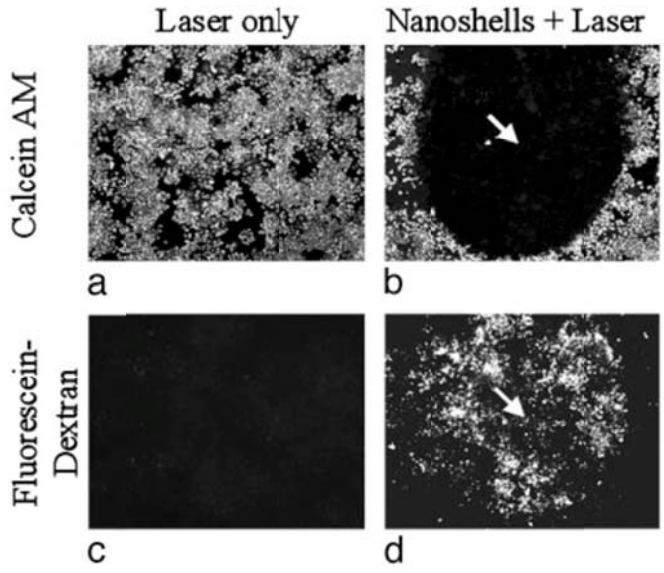

Figure 9. Plasmonic laser photothermal treatment of breast cancer cells (SK-BR-3) exposed to 35 W/cm^2 laser intensity for 7 min. Unlabeled cells maintained both cell viability, as is shown by (a) calcein fluorescence and (c) membrane integrity, indicated by the lack of 10 kDa FITC-dextran uptake. Cells labeled with nanoshells underwent photothermal destruction within the laser spot as shown by (b) calcein fluorescence and (b) the cellular uptake of 10 kDa FITC-dextran. Reproduced, with permission, from [97].

Nanospheres, the most fundamental particle geometry, were exploited for their large resonant absorptions in the visible portion of the electromagnetic spectrum and ease of production. It has been found by a number of researchers, that particles of 30-40 nm sizes produced maximal temperatures when irradiated with light tuned to their plasmonic resonance [32]. The El-Sayed group experimentally labeled HSC 3 and HOC 313 cells (human oral squamous cell carcinoma), in an *in-vitro* setting with 35 nm gold nanospheres conjugated to anti-EGFR antibodies. Dark-field microscopy was used to verify that immunotargeted nanoparticles homogeneously bind to malignant cell types with 600 times more affinity than that of nonmalignant cell types [4]. Labeled cells were irradiated with a CW, 514 nm wavelength, argon laser, which overlaps the surface plasmon absorption of the spherical nanoparticles (520 nm peak absorption wavelength). The laser light was focused to a 1 mm spot size and the sample was irradiated for 4 min. A threshold intensity of 19 W/cm^2 was determined to kill labeled, cancer cells, which is less than half the laser intensity needed to kill unlabeled, nonmalignant cells [99,100].

Gold nanorods, originally developed by the El-Sayed group [12,62], provide great potential for photothermal ablation in the NIR wavelength regime. By tuning the ratio of the transverse to longitudinal lengths, the strong longitudinal absorption band is shifted into the NIR

wavelength regime, which allows for photothermal therapy with maximal penetration of light through tissue. This is a regime in which single gold nanospheres have shown low levels of absorption. Since their size is considerably smaller than other engineered particle types such as nanoshells, they have the potential to penetrate deeper into tissue structures through passive means. Albeit, there is a strong dependence on laser absorption with nanorod orientation to the incident electric field, which is currently uncontrollable with current targeting methods.

The El-Sayed group has shown evidence for the nanorod-assisted photothermal ablation of the human oral squamous cell carcinoma types HOC 313 clone 8 and HSC 3. Through the capping of nanorods with poly(styrenesulfonate) (PSS), it is possible to functionalize the nanorod surface. PSS-capped nanorods have a strong binding ability to molecular macromolecules. Cells labeled *in-vitro* with gold nanorods conjugated to anti-EGFR antibodies were found to be irreversibly damaged after a 4 minute exposure to CW Ti:sapphire laser light at 800 nm. The threshold intensity to kill cancer cells was found to be 10 W/cm^2, which is lower than that found for nanospheres and nanoshells, resulting from a higher particle absorption cross-section [5]. The Wei and Cheng group have shown extensive membrane damage using folate ligand functionalized nanorods [26]. *In-vitro* labeled KB cells, a malignant cell line derived from oral epithelium, were irradiated with 81.4 seconds of CW, 765 nm laser light. Severe blebbing, associated with Ca^{2+} influx into the cell, was found at a threshold intensity of 389 W/cm^2. When the nanorods were internalized into the cells, cell death required approximately 10 times more laser intensity.

Table 1: Summary of nanoparticle-based CW-laser phototherapies performed on cells *in vitro*.

Nanoparticle Characteristics	**Laser Parameters:** Wavelength	**Exposure Parameters:** Exposure time Irradiation values Total energy per area	**Results**	**Ref**
Sphere				
35 nm, gold 520 nm plasmon resonance functionalized with αEGFR	514 nm	4 min 19 W/cm^2 4.56 kJ/cm^2	Four times greater energy required to kill unlabeled normal cells compared to labeled malignant cells.	2006 [94]
Shell				
10 nm gold shell 110 nm silica core 820 nm plasmon resonance functionalized with αHER2	820 nm	7 min 35 W/cm^2 14.7 kJ/cm^2	Cell death was confined to the laser/nanoshell treatment area. Exposure to NIR along did not kill cells.	2003 [97]
Rod				
3.9 Aspect ratio, gold 800 nm plasmon resonance functionalized with αEGFR	800 nm	4 min 10 W/cm^2 2.4 kJ/cm^2	Half laser energy required to kill labeled malignant cells compared to normal cells.	2006 [5]

4.1.2. *In-vivo animal studies:*

In animal studies, Gobin *et al.* [101] studied the efficacy of both the direct injection of nanoshells into the tumor and passive accumulation of nanoshells into tumors via enhanced blood vessel permeability and retention. Female nonobese diabetic CB17-Prkd c SCID/J mice were inoculated in the right and left hind leg with canine TVT cells. PEG-passivated NIR-absorbing gold-silica nanoshells were injected interstitially 5 mm into the tumor volume. The nanoshell-ladened tissue was exposed for 6 minutes to a total intensity of 4 W/cm^2, 30 minutes after injection. Utilizing magnetic resonance thermal imaging, the temperature profile was monitored during nanoshell exposure to NIR light. It was shown that the average maximum temperature sustained in the tissue increased by 37.4 ± 6.6°C, causing irreversible tumor damage [97].

Direct injection of nanoshells to the place of interest is not possible in every case, as tumors or lesions can be embedded deep within a tissue structure. Researchers at Rice University investigated the uptake of nanoshells via passive accumulation from the blood stream. Rapid angiogenesis during tumor formation causes many of the newly formed vasculature to be leaky, allowing macromolecules to preferentially extravasate into tumor tissue. It is from this vasculature that nanoparticles can enter into the tumor via standard blood flow. Nanoshells of 60-400 nm size have been shown to extravasate and accumulate in many tumor types. After photothermal therapy, complete tumor regression was seen in the murine model within 10 days

following heat treatment. More promising is the fact that no tumor regrowth was seen after 60 days. When compared to control studies (no treatment and laser treatment alone), survival times for mice inoculated with nanoshells were significantly improved; 83% of mice survived 7 weeks post nanoshell phototherapy compared to under 20% for the control groups.

4.2. Pulsed Laser Plasmonic Phototherapy

Pulsed laser irradiation provides a platform for the confinement of photoactivated processes. In this section, we describe the various approaches taken by researchers to localize laser damage to subcellular targets. Table 2 presents a listing of pulsed PLP results found in the literature. To introduce the concept of confinement, we begin our discussion with a presentation of heat confinement to disrupt molecular macromolecules (e.g., proteins). We then proceed to describe cancer treatments mediated by photoinduced hyperthermia. Next we describe higher energy nanoparticle irradiation where bubble formation is induced in both single and multiple particle systems. Cellular disruption through explosive particle fragmentation and nonlinear absorption mechanism is next described. Lastly we discuss the near-field ablation of cellular membranes.

4.2.1. *Localized thermal damage (hyperthermia):*

Localized thermal damage of absorbing molecules by pulsed laser irradiation was first proposed by Anderson and Parrish [102]. They showed that laser-induced thermal damage is confined to the endogenous absorbing structure when the pulse duration is shorter than the thermal relaxation time of the structure. In their original work, they utilized the interaction between subcellular pigment microparticles with short pulse laser radiation to induce cell lethality. This simple concept has led to an explosion of technologies in hair and port wine stain removal and acne reduction, for example. The manipulation of subcellular material requires irradiation by lasers with pulse durations of nanoseconds and less.

The concept of localized thermal damage was next extended to the use of exogenous micro- and nanoabsorbers for controlled subcellular and cellular membrane manipulations by Lin *et al.* [103] and Huttman *et al.* [88]. They demonstrated thermal effects with spatial confinements of less than 50 nm utilizing highly absorbing polystyrene latex microspheres loaded with iron

oxide and immunogold nanospheres irradiated with nanosecond and picosecond laser pulse durations.

At their plasmonic frequency, gold nanoparticles have strong absorption properties, allowing for large surface temperature generation with excitation fluences as low as 1 mJ/cm^2. As a quick example, we can calculate (using the heat transfer model with interface conductance) that a gold nanosphere of 30 nm diameter irradiated by a single, 35 ps laser pulse at 527 nm wavelength and fluence 1 mJ/cm^2 will absorb approximately 10 fJ of energy, giving a maximum particle temperature of approximately 540 K (Fig. 10(a)). Figure 10(b) theoretically demonstrates that the particle will heat the surrounding medium with a spatial confinement of approximately 5 nm.

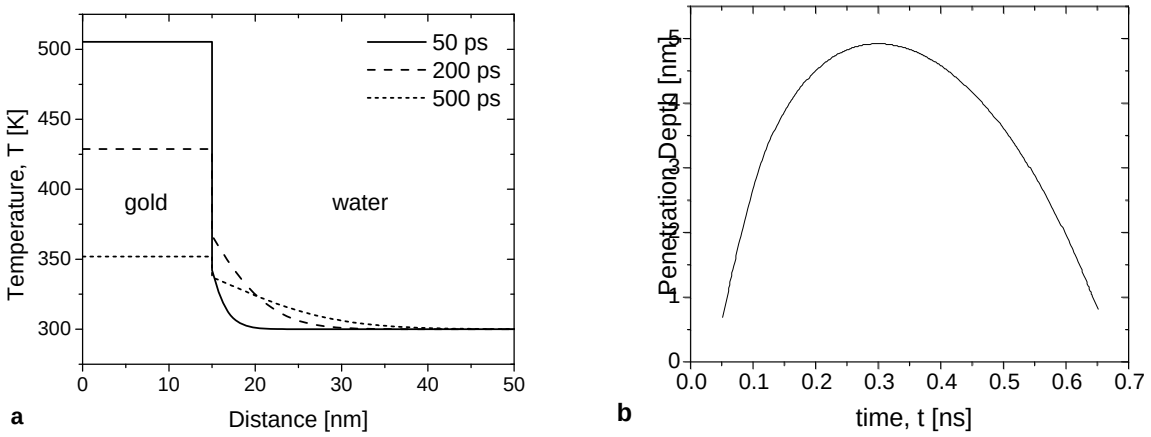

Figure 10. Thermal heating properties of a 30 nm spherical gold particle irradiated with 35 ps laser light at a 527 nm wavelength and fluence of 1 mJ/cm^2. (a) Temperature profile of the particle and water at 50, 200, and 500 ps after the application of the laser pulse. (b) Penetration depth of high temperatures (down to the 1/e value of the water temperature rise, 330 K) into the surrounding water.

The concept of spatial confinement using picosecond laser heated nanoparticles was studied via protein denaturation and subsequent inactivation. In their initial study, Huttman *et al.* [88] characterized the extent of the spatial confinement by changing the distance between the target and the particle surface. Initially, 15 nm gold nanospheres were directly coupled with the protein alkaline phosphatase (aP). The aP protein denatured when 10^4 pulses of 35 ps, 527 nm wavelength laser light of fluence 50 mJ/cm^2 per pulse were applied. On the other hand, when the aP protein was indirectly coupled to the nanoparticle via an antibody linker (~ 5-10 nm long), irradiation of the particle system with the same parameters did not inactivate the protein.

Questions arose on whether the linker was inactivated instead of the protein of interest, resulting in aP dissociation from the linker. However, they came to a conclusion that the aP protein would not diffuse away from the particle by any appreciable distance during the nanosecond long heating cycle (see Fig. 10(b)) and that localized heating induced by the nanoparticle was most likely responsible for aP inactivation. Photochemical generation of reactive species and surface enhanced two photon absorption were also cited as possible damage mechanisms.

To elucidate the temperature at which protein unfolding and inactivation occurs, Huttman *et al.* [104] performed a set of protein inactivation studies by laser-induced temperature jumps. Additionally, they modeled particle heating dynamics to determine whether the particle can reach temperatures high enough to cause protein inactivation. Here, free chymotrypsin in water was heated via irradiation from 2.1 μm laser light of varying pulse durations, to temperatures between 370–470 K. Chemotrypsin inactivation occurred within 300 μs at a temperature of 380 K. The unfolding of chemotrypsin with respect to the generated heat followed the Arrhenius equation down to pulse durations of 330 μs. From theoretical temperature calculations of nanospheres after laser irradiation (using model developed by Goldenberg and Tranter [105]), they determined that temperatures generated by the particle after irradiation with pico- and nanosecond laser pulses of fluences ranging from tens to a few hundreds mJ/cm^2 would indeed be enough to induce protein inactivation. One concern that arises from using the Goldenberg and Tranter model is that it does not take into account the interface conductance. Due to the phonon-phonon mismatch, there will be a temperature drop at the boundary. As such, higher fluences than reported might be necessary to generate water temperature sufficiently high enough to induce protein inactivation.

To verify the hypothesis that thermal processes are indeed the mechanism of protein inactivation, we need to refer to the studies discussing the mechanisms of explosive boiling. Using nanosecond time-resolved microscopy, Lin *et al.* [103] determined that surface tension permits high temperatures to exist at the nanoparticle surface without vaporizing the surrounding water. The extreme particle temperature rise occurs as a result of the high rate of energy deposition. As was explained earlier, the rapid deposition can cause superheating in a thin layer of surrounding water instead of the expected phase change at the normal boiling temperature. If the vapor pressure overcomes the surface tension, the superheated liquid undergoes an explosive phase change. Explosive boiling typically occurs when the temperature of the liquid reaches 90%

of its critical temperature (647 K) [77,80,83,84]. Since chymotrypsin can be denatured within 300 μs at temperatures below 380 K, which is well below the critical temperature for explosive boiling, one can conclude that in the above examples protein inactivation cannot be as a result of explosive boiling and is most likely due to hyperthermic processes. Additionally they argued that if mechanical damage by explosive boiling were the cause, aP proteins indirectly coupled to the nanoparticle would also be damaged during irradiation.

Pulsed photothermal therapy for target tumor therapy has also been demonstrated in the NIR wavelength regime using functionalized nanocages and nanorods. Chen *et al.* [60] experimentally demonstrated the photothermal destruction of SK-BR-3 cells labeled with nanocages after the application of 20 ps, 810 nm laser light (82 MHz repetition rate) for 5 minutes. An average threshold intensity of 1.5 W/cm^2, which corresponds to a fluence of 18 nJ/cm^2, was determined for irreversible membrane damage. Takahashi *et al.* [106] reported HeLa cell death in the presence of phosphatidylcholine-passivated gold nanorods when exposed to 2 minutes of 6-9 ns laser pulse of 1064 nm wavelength with a pulse fluence of approximately 280 mJ/cm^2. Albeit, with pulsed lasers, particle reshaping to the more thermodynamically stable spherical shape can be induced. Link *et al.* [87] experimentally studied nanorod reshaping for both nanosecond and femtosecond lasers. They found that the energy threshold required for complete melting of the nanorods is two orders of magnitude less when using femtosecond laser pulses compared to the required energy with nanosecond laser pulses. This difference is attributed to the decreasing absorption efficiency and increased heat dissipation from the particle to the surroundings during the pulse duration in the case of nanosecond laser pulses. Takahashi *et al.* [107] proposed a method of using nanorod reshaping to mediate the finality of phototherapy. They found that after the application of 890 mJ/cm^2 fluence pulses for 2 minutes, the nanorod transforms from a rod to spherical shape. It was concluded that nanorod reshaping during therapy will prevent continued cell death to surrounding normal tissue due to significantly reduced absorption effects in the NIR while killing the intended target.

4.2.2. *Bubble formation:*

A vapor bubble will rapidly expand around the particle if the amount of energy absorbed by the nanoparticle is high enough for the initial high vapor pressure to overcome the surface tension of the liquid, which is inversely proportional to particle size [104]. Due to low heat

transfer across the vapor, the bulk of surrounding material remains at ambient temperature. A shock wave and traveling high-pressure waves will be generated as a result of the expansion and the collapse of bubbles, which is proposed to be the cause of cellular membrane disruption [108]. When cavitation bubbles form, thermal denaturation most likely plays a minor role in cellular death [89]. It is found that damage due to cavitation is highly localized and only cells that have internalized particles or membrane-bound particles are killed upon laser exposure.

Pitsillides *et al.* [89] were the first group to experimentally demonstrate the use of bubble formation around nanoparticles as a method of selectively introducing exogenous macromolecules into the cellular cytoplasm through the plasma membrane. They investigated transient pore formation in the plasma membrane by the irradiation of 30 nm gold nanospheres with 100 pulses of 20 ns, 565 nm wavelength laser light at a laser fluence of 500 mJ/cm^2. Membrane permeability was measured through the increase in the cellular uptake of the permeability probe 10 kDa FITC-Dextran. It was found that 500 gold particles conjugated to plasma membrane were most effective in killing 95% of cells under the aforementioned laser irradiation conditions. This reported particle loading is approximately 10 times less than what is necessary with CW techniques. When compared to the other photoactivated therapies such as Photodynamic Therapy, approximately 2000 times less cellular loading of immunotargeted particles is necessary for a similar level of performance [109].

The ability of pulsed laser irradiated nanospheres to induce localized damage through nano-scale bubble formation was further studied by Yao *at al.* [92]. Their goal was to inflict temporary permeability in the plasma membrane without causing cell death as a way to assist in gene transfection and gene therapy. To prove the concept, 30 nm particles conjugated to membrane specific antibodies were delivered to the plasma membrane of the cancer lines L428 (Hodgkin's disease) and 299 (Karpas Lymphoma). They demonstrated the efficient transfer of relatively small exogeneous molecules in the cytoplasm using 6 ns laser pulses at 532 nm wavelength. Permealization and resealing were studied through variations in laser parameters, gold concentration, and membrane proteins. A transfection efficiency of 68% was achieved with only 27% cell death after exposure to 5 laser pulses of 120 mJ/cm^2 fluence, when the cell was labeled with 1.1 x 10^5 nanoparticles.

With decreasing pulse duration, the energy necessary to heat the surrounding water to 90% of its critical temperature is reduced and thus greater is the heat damage confinement. As a

quick comparison, we can estimate the energies required to create bubbles around a 30 nm gold nanosphere irradiated by picosecond and nanosecond laser pulses using the heat diffusion model described in the previous section. Figure 11 presents a theoretical comparison between two cases: (1) heating with a single, 35 ps laser pulse at 527 nm wavelength (conditions similar to experiments of Huttman *et al.* [88]) and (2) heating with a single, 20 ns laser pulse at 565 nm wavelength (conditions similar to experiments of Pitsillides *et al.* [89]). Both cases were modeled using the heat transfer model with interface conductance. As can be seen in Fig. 11, the application of picosecond laser pulses requires 72 times less energy for the particle to reach the 90% of the critical temperature of water than is required by nanosecond laser pulses. While the heat confinement is approximately 5 nm for ps-laser heated particle, it reaches 17 nm for ns-laser heated particle.

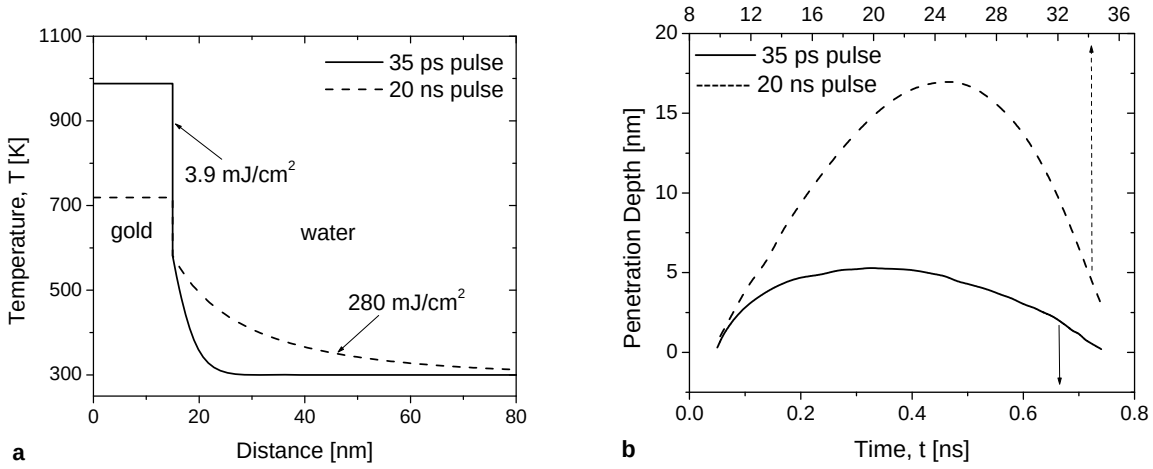

Figure 11. Comparison of laser fluences necessary to bring water to 90% of its critical temperature at 580 K around a 30 nm spherical gold particle exposed to picosecond (35 ps, λ = 527 nm) and nanosecond (20 ns, λ = 565 nm) laser pulses with a Gaussian temporal profile: (a) Temperature profile of the particle and water at 22 ns and 125 ps for the picosecond and nanosecond pulses, respectively, when the peak water temperature occurred. (b) Heat penetration depth as defined by the 1/e location of water temperature rise (~ 400 K).

Finally, cell membrane disruption by cavitation bubbles can additionally be mediated by nanorods, due to their increased efficiency in NIR absorption and photothermal energy conversion. Tong *et al.* [26] demonstrated photothermolysis of KB cells through the laser interaction of nanorods functionalized with folic acid to the plasma membrane. After the application of 765 nm, 200 fs laser light at a 77 MHz repetition rate with an energy deposition

rate of 9.7 pJ/pulse (for a 1.2 NA objective lens we calculate a fluence of 3 mJ/cm^2 per pulse) deposited during 10 seconds, the labeled KB cells produced clearly visible membrane blebbling. KB cells loaded with internalized nanorods required 6 times more laser fluence to induce cellular damage. The large increase in necessary fluence for cell death between membrane-labeled and internalized nanorods demonstrates the high localization of induced photodamage.

4.2.3. *Overlapping bubble formation:*

Bubbles can be overlapped for enhanced photodisruption of cancer cells. Overlapping bubbles can be created by gold nanosphere aggregates. A variety of aggregation methods have been proposed, including: (1) clustering secondary monoclonal antibody labeled nanospheres on a targeted single nanosphere [16,17], (2) targeting naturally clustered cancer biomarkers[3,110], and (3) concentrating nanoparticles with viruses and vesicles [93.

Enhanced bubble formation occurs due to overlapping bubbles from individual particles within an aggregate, generating one large bubble around the aggregate [17,111]. Lapotko *et al.* [17] experimentally presented evidence for selectively induced microbubbles in leukemia cells labeled with large aggregates and not those labeled with individual particles and small aggregates. A bubble formation threshold of 600 mJ/cm^2 was found for large nanoparticle aggregates under single pulse, 532 nm, 10 ns laser irradiation conditions.

Nanoparticle aggregates also red-shift the plasmon resonance into the near-infrared wavelengths, leading to enhanced optical and thermal amplification. Zharov *et al.* [112] and Larson *et al.* [113] provided experimental evidence for enhanced bubble formation in the vicinity of large nanosphere aggregates when irradiated by NIR laser light. Both groups showed a reduction in the bubble formation threshold from 600 mJ/cm^2 down to 400 – 500 mJ/cm^2 with the application of a single nanosecond laser pulse in the NIR. The role of multiple nanosecond laser pulses was also studied by Zharov *et al.* [112]. They irradiated nanosphere labeled cells with 500 pulses further reducing the bubble formation threshold to 80 mJ/cm^2.

4.2.4. *Fragmentation of nanoparticles:*

Fragmentation and thermal explosion of nanoparticles is an additional mechanism that can induce localized damage (either desired or unwanted) to cellular material in the vicinity of the particles. Desired thermal explosion of particles may accompany plasma or bubble formation,

further decreasing the threshold for cell death. However, unwanted damage to surrounding healthy cells because of the uncontrolled nature of the extent of damage after the particle fragmentation or explosion can occur. In addition, once the particle is reshaped due to fragmentation, the efficiency of PLP is greatly reduced. Shape transformations shift the peak of the plasmon resonance, significantly reducing the designed laser absorption efficiency of particles and thus the efficacy of PLP.

With the application of short duration laser pulses, fragmentation and thermal explosion of nanoparticles may occur. A large degree of the absorbed energy will initially remain in the particle, heating it to very high temperatures, since the heat diffusion to the surrounding tissue is minimized during rapid heating with short duration laser pulses. The mechanism of fragmentation, however, may be different for different pulse durations. Link *et al.* [87] discuss the differences in fragmentation mechanisms of nanorods irradiated by femtosecond and nanosecond pulses. Their TEM images show that the fragmented particles are mostly irregularly shaped in the case of femtosecond pulses while nearly spherical shapes are observed in the case of nanosecond pulses. It is suggested that the fragmentation of particles exposed to nanosecond pulses occurs as a result of thermal heating and melting processes. On the other hand, when exposed to femtosecond pulses, a rapid particle explosion can occur as a result of multiphoton ionization where the lattice is still cold and this would explain the irregularly shaped fragmented particles. Letfullin *et al.* [108] theoretically calculated the threshold fluence for thermal explosions of both gold nanospheres and nanorods when irradiated with nanosecond pulses at the plasmon resonance. They found a threshold fluence of approximately 40 mJ/cm^2 for gold nanospheres, which can be reduced to fluences down to 11 mJ/cm^2 for relatively large gold nanorods.

4.2.5. *Nonlinear absorption induced PLP:*

Particles can exhibit enhanced heating properties due to nonlinear absorption effects such as two photon absorption and second harmonic generation. The principle has been exploited by a variety of groups to achieve intracellular molecular manipulation and to locally disrupt cellular membranes. Csaki *et al.* [24] utilized two-photon absorption by silver-gold heterodyne spherical particles conjugated to ssDNA strands to photodisrupt targeted chromosomal molecular material with 800 nm laser light with laser fluences of tens of mJ/cm^2. With this technique, large-scale

parallelization of gene-specific molecular surgery utilizing metal nanoabsorbers can be achieved. Envisioned applications include DNA analytics as well as single cell manipulation. Mazumder *et al.* [91] targeted spherical 5 nm gold particles to chromatin to investigate the mechanical coupling of chromatin to the nuclear architecture. Perturbation of the chromatin assembly was performed with 835 nm, pulsed laser light at 56 mW focused at the nucleus for 3 seconds (corresponding fluence is 15 mJ/cm^2 per pulse). Using the high spatial localization of nanoparticle generated heat; their findings showed the direct differential coupling of heterochromatin to specific cytoskeletal network elements. Huang *et al.* [100] found that with large particle loading on the plasma membrane of HSC oral cancer cells, the formation of large particle aggregates led to enhanced, nonlinear absorption processes and reduced the threshold fluence to cause a 20-fold increase in the number of cells killed.

4.2.6. *Plasmonic laser nanosurgery (PLN):*

Femtosecond laser pulses can initiate plasma-mediated ablation with only a few tens of nano-Joules of energy due to their high peak intensities [114,115,116,117]. Ablation with very-low pulse energies becomes especially important when dealing with live cells and organisms having minimal tolerance to temperature increases. The intense near-field scattering effect of gold nanoparticles in the NIR wavelength regime can be utilized to induce plasma formation in the vicinity of the particle for high precision cellular membrane disruption.

Figure 12 presents the first experimental evidence of the concept of plasmonic laser nanoablation (PLN) where the enhanced plasmonic scattering in the near-field of gold nanoparticles can be used to vaporize both solid materials and biological structures with nanoscale resolution. Eversole *et al.* [118] experimentally demonstrated nanocrater formation on silicon by the enhanced ultrafast laser scattering in the near-field of 150 nm gold nanospheres. As previously shown in Fig. 3(a), the chosen particle size maximizes near-field scattering at the 780 nm laser wavelength, while minimizing absorption effects (the ratio of near-field scattering to linear absorption is approximately 60 as shown in Fig 3(b)). Figures 12(b) and (c) provide experimental evidence of material removal after plasmonic laser ablation of silicon. The generated crater follows the theoretical scattering pattern, confirming crater generation is indeed by near-field scattering effects.

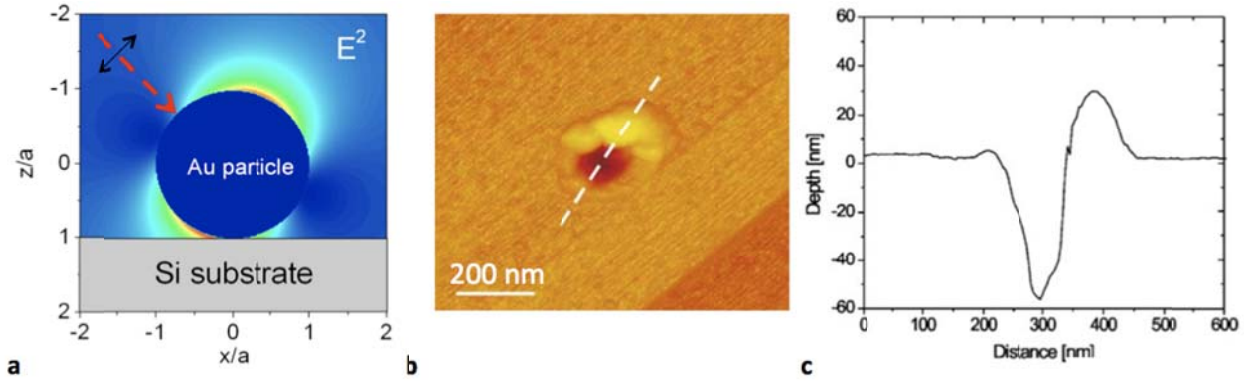

Figure 12. Plasmonic Laser Nanoablation (PLN) technique proposed by Ben-Yakar group. (a) Theoretical calculations showing the field intensity around a gold nanosphere deposited on silicon substrate. The large enhancement of the ultrafast laser scattering in near-field of a gold nanoparticle can be used to ablate the silicon substrate right underneath the particle. (b) Experimental evidence for PLN showing nano-craters on silicon ablated using a 150 nm, spherical, gold nanoparticles; AFM image of nanocrater generated by a 88 mJ/cm^2 average fluence laser pulse at 780 nm having p-polarization at 45° incident angle, and (c) corresponding cross section along the dotted white line.

The Ben-Yakar lab group is currently extending plasmonic laser nanoablation to cellular membrane ablation. In initial results, MBA-MB-468 epithelial breast cancer cells were labeled with 80 nm gold nanospheres functionalized with anti-EGFR antibodies. Figure 13(a) provides a multiphoton luminescence image of labeled cells at 850 nm, which provides only a weak autofluorescence signal relative to the luminescence from the particles. Labeled cells, irradiated with 80 MHz repetition rate pulses of 18 mJ/cm^2 fluence for 10 sec at 760 nm wavelength, showed reduced membrane integrity, as seen by the uptake of 10 kDa FITC-dextran in Fig. 13(b). Unlabeled cells required 8 times more laser fluence for the membrane integrity to be reduced. Since linear absorption by the particle is negligible at the laser wavelength (the ratio of near-field scattering to linear absorption is approximately 55), membrane disruption was attributed to the formation of a low-density plasma in the particle near-field resulting from intense near-field scattering.

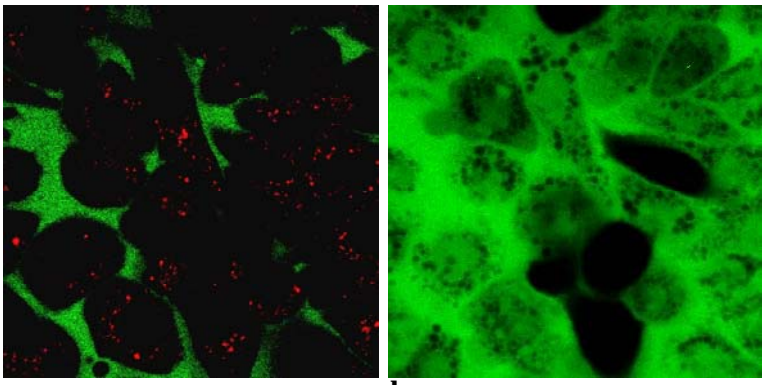

a b

Figure 13. Plasmonics laser nanoablation of cancer cells (MDA-MB-468) labeled with 80 nm gold nanoparticles functionalized with anti-EGFR antibodies. (a) Nanoparticles in red, imaged at 850 nm wavelength through multiphoton luminescence, and cell membrane impermeable dye (10 kDa FITC-Dextran) in green, imaged at 760 nm wavelength. (b) Fluorescence images show reduced membrane integrity, as seen with the intake of FITC-Dex, after the application of 80 MHz laser pulses of 18 mJ/cm^2 for 10 sec.

Table 2: Summary of pulsed Plasmonic Laser Phototherapies (PLP).

Nanoparticle Characteristic	Laser Parameters: Pulse duration Wavelength Repetition Rate	Exposure Parameters Number of pulses Irradiation values	Results	Ref
Nanosecond Pulses				
Sphere				
30 nm, gold	20 ns pulse duration 565 nm wavelength	100 pulses 500 mJ/cm^2 per pulse	500 particles/cell 95% cell death	2003 [89]
30 nm, gold	6 ns pulse duration 532 nm wavelength	5 pulses 15 mJ/cm^2 per pulse	68% transfection efficiency 27% cell death 1.1 x 10^5 particle/cell labeling	2005 [92]
Sphere Aggregates				
30 nm, gold >200 nm cluster	10 ns pulse duration 532 nm wavelength	1 pulse 600 mJ/cm^2 per pulse	Cell death only found when large clusters present Bubble formation detected	2006 [17]
40 nm, gold >300 nm cluster	12 ns pulse duration 1064 nm wavelength	500 pulses 80 mJ/cm^2 per pulse	Cell death only found when large clusters present	2005 [112]
Shell Aggregates				
45 nm, γ-Fe_2O_3/Au 540 nm plasmon resonance	7 ns pulse duration 700 nm wavelength	1 pulse 400 mJ/cm^2 per pulse	Observed reduced calcein AM fluorescence	2007 [113]
Rod				
5.9 Aspect ratio, gold 900 nm plasmon resonance	6-9 ns pulse duration 1064 nm wavelength 10 Hz repetition rate	1,200 pulses 280 mJ/cm^2 per pulse	Studied trypin blue uptake	2006 [106]
Picosecond Pulses				
Sphere				
15 nm, gold	35 ps pulse duration 527 nm wavelength 1 kHz repetition rate	10^4 pulses 50 mJ/cm^2 per pulse	aP protein inactivation	2002 [88]
Cages				
45 nm edge length 3.5 nm wall thickness 3:1 gold/silver ratio 810 nm plasmon resonance	20 ps pulse duration 810 nm wavelength 82 MHz repetition rate	5 min exposure time 18 nJ/cm^2 per pulse	Studied calcein AM and EthD-1 uptake	2007 [60]
Femtosecond Pulses				
Sphere				
5 nm, gold	80 MHz 835 nm wavelength	3 sec exposure time 15 mJ/ cm^2 per pulse (cited 56 mW and 2.5 μm spot size)	Chromatin assembly disrupted *in-vivo*	2007 [91]
80 nm, gold 600 nm plasmon resonance	80 MHz 760 nm wavelength	10 sec exposure time[a] 18 mJ/cm^2 per pulse (20 mW with 0.95 NA	Studied 10 kDa FITC-dextran uptake	2008 presented here

		lens)		
Sphere Aggregates				
30 nm, gold 540 plasmon resonance after cellular attachment	1 kHz 800 nm wavelength	2 min exposure time 140 μJ/cm^2 per pulse (cited 1.1 mW and 1mm spot size)	Quadratic dependence of photothermal efficiency on laser power indicates multiphoton process	2006 [17]
Silver Shell				
40 nm silver shell 20 nm gold core 400 nm plasmon resonance	800 nm wavelength 80 MHz repetition rate	Line scan 7-30 mJ/cm^2	Cut chromosomes	2007 [90]
Rod				
765 nm plasmon resonance	200 fs pulse duration 765 nm wavelength 77 MHz repetition rate	10 sec exposure time[a] 3 mJ/cm^2 per pulse (cited 9.7 pJ/pulse with 1.2 NA lens)	Nanorods localized on membrane Studied Ca^{2+} intake	2007 [26]

[a] Laser beam is scanned

4.3. Summary of Plasmonic Laser Phototherapy

In conclusion, we have summarized plasmonic phototherapy of biological materials and how it can be utilized for a highly selective treatment of cancer. For the most part, plasmonic phototherapy has centered on the use of the strong absorption properties of gold nanostructures to kill cancer via hyperthermia, bubble formation, particle and fragmentation. Some more recent technology has begun to exploit the intense near-field scattering properties of gold nanoparticles for plasma-mediated ablation. By changing particle geometry and composition, applications across the visible and near-infrared wavelength regimes have been developed. Additionally, depending upon the pulse duration, the region of photodamage can be controlled. CW irradiation allows for large-scale tissue destruction, while short pulses can be yielded to manipulate finer structures in tissues and cells. With further refinements in cell labeling and laser delivery to tissues, various nanoparticle-based laser phototherapies, including photothermal, photomechanical (bubble formation or particle fragmentation), and photoablation (plasma-mediated) techniques, have a strong prospect to become gold standard in various cancer treatments.

5. Summary

Noble-metal particles have highly tunable optical properties and as such have shown great promise as a highly sensitive and cost effect multimodal tool for the screening, diagnosis, and

therapy of cancer. In this chapter we primarily discussed the role of Plasmonic Laser Phototherapy (PLP) as a novel nanoparticle-based laser cancer treatment. Researchers have shown that by conjugating molecular specific bioagents (e.g. antibodies and ligands) to the particle surface, a variety of potential cancer targets exist. Using nanoparticles of different sizes, geometries, and compositions, therapy can be tuned to a variety of laser wavelengths ranging from the visible to NIR regions of the electromagnetic spectrum. The fundamental spherical particle strongly absorbs laser light in the visible wavelength range. To shift the plasmon resonance to NIR wavelevengths, where light penetration in tissue is maximized, heterodyne and asymmetric particles have been developed. Treatment of surface lesions would most benefit from lower wavelength laser light, while large-scale tumors require NIR laser light (light penetration on the order of several centimeters depending upon tissue type). Additionally, varying laser pulse durations have permitted researchers to define the degree of heat confinement around the particle during treatment. CW lasers are typically utilized to treat bulk tissue structures, while pulsed lasers can be utilized to confine thermal and subsequent thermo-mechanical effects/damages to the cellular level. Through variation of each of the parameters discussed, it is possible develop a large range of cancer therapies in a variety of tissues.

With CW lasers, *in-vivo,* large-scale tumor reduction was verified using nanoshell phototherapy. Here, complete tumor regression was found 10 days after treatment with no regrowth after 60 days. Utilizing active binding methods of nanoparticles to cancer cells, thresholds for photodestruction were determined to be 35 W/cm^2 for nanoshells, 19 W/cm^2 for nanospheres, and 10 W/cm^2 for nanorods. With pulsed lasers, the manipulation of proteins, organelle membranes, and DNA has been achieved. Large amounts of energy are absorbed by the particle within a short time duration, significantly reducing the required fluence to generate large temperature increases. Femtosecond laser pulses require fluences an order of magnitude smaller compared to that needed with nanosecond pulses. As such, heat is confined to the particle near-field, providing a platform for true *in-vivo* nanoscale manipulation of biological substances. PLP has shown great promise for the selective treatment of cancer as well as other diseases with both CW irradiation and pulsed laser techniques. We anticipate that the technique will be successfully applied to the clinical setting as a number of parameters are optimized.

6. Future Perspectives:

PLP is a novel nanoparticle-based laser technology for the therapy of cancer cells, viruses and bacteria and genetic manipulation that has been maturing over the past few years. Albeit, a number of parameters still need optimization (as shown in Table 3) for the technique to find application in a clinical setting. Both particle and optical parameters are functions of the clinical application and need to be optimized accordingly. In this section, we will briefly define possible parameter optimizations that will complement ongoing *in-vitro* and *in-vivo* experiments to fully mature PLP.

Table 3: Parameters important to understand for the application of PLP in a clinical setting

1. Particle Dynamics
a. *Stability*: ability to circumvent physiological system without removal from body
b. *Biocompatibility*: no adverse chemical reactions with physiological environment
c. *Optical*: ability of particle to optimally absorb and scatter incident laser light
d. *Clearance after therapy*: particle removal through lymphatic system
2. Particle Functionalization
a. *Stability*: dissociation of molecular specific bioagents from particle
b. *Delivery*: transport of particles to desired location through topical delivery or intravenous injection
c. *Biomarker targeting*: desired location of particle in tissue/cell and distance from choice target
d. *Spatial localization*: functional method for bringing the particle to desired distance to the target
3. Laser Irradiation
a. *Optical spatial localization*: laser parameters defining the optical localization for a given geometry
b. *Delivery*: ability to bring laser light to desired location
c. *Light Penetration*: light penetration in tissue to desired depth with minimal scattering and absorption
4. Multifunctionalization
a. *Therapeutic*: use in combination with conventional photodynamic therapies
b. *Imaging*: development of "smart particle" for both *in-vivo* imaging and therapy

PLP has a number of distinct advantages that make it compatible for the treatment of disease:

1) Nanoparticles spatially confine thermal and mechanical effects, providing;
   a) Highly precise photodisruption of cells or subcellular targets
   b) Low fluence irradiation with minimal disruption to surrounding, normal tissue
2) Their optical properties are tunable to NIR wavelengths, allowing;

a) Deep tissue penetration
b) Possible use of non-linear effects to improve selectivity
c) Freedom to choose between absorption and near-field scattering dynamics

3) Easy nanoparticle functionalization methods provide:
   a) Enhanced targeting to cancer biomarkers with high selectivity
   b) High throughput phototherapeutic process
4) Allows for combined imaging and therapy:
   a) Through scattering and bright multiphoton luminescence, nanoparticles can additionally double as image contrast agents
   b) Image guided therapy

Through confinement of thermal and mechanical effects to the target tissue or cell, it is possible to treat a particular region of interest with high specificity, which is extremely important in cancer therapy. Furthermore particles can be functionalized to target cancer biomarkers with high specificity. Together these two properties provide the highest level of therapeutic selectivity of cancer cells. Additionally particles can act as strong contrast agents for differentiation of normal versus cancer cells, further allowing for image guided therapy. As a quick example, for the treatment of a cancer mass in the brain (e.g. medulloblastoma) it is of utmost importance to kill the tumor, while leaving normal, healthy brain tissue intact, such that the therapeutic process does not disrupt important brain functions (e.g. visual and motor controls). Such highly precise phototherapy can be achieved only through image guided therapy with the aid of plasmonic gold nanoparticles. Additionally, through variation in laser pulse duration, the confinement of damage to biological material surrounding the particle can be controlled. Finally, the optical response of the particle is highly tunable (visible to NIR). The tunability to NIR wavelengths is especially important for reaching tumors embedded deep within a tissue.

A variety of important parameters, listed in Table 3, still need attention in the development of PLP. In many cases, these parameters are defined by the biology of the clinical situation. To date, a large portion of the use of PLP has only been tested in an *in-vitro* setting, which only proves the ability of the technique to provide an alternative means of cancer removal. As PLP is tested in animal models and particle-laser interaction models are refined, these

important optical and particle parameters will be realized, making the technique applicable for *in-vivo* cancer removal.

Particle design parameters, both dynamic and functional, need to be optimized to meet clinical needs. First and foremost, for the clinical setting to become reality, developed bioconjugates must have a shelf life long enough to be useful in ambient conditions found in clinics. Current bioconjugates typically have shelf lives of 2-3 days in 4°C temperatures before the bioagent dissociates from the nanoparticle surface. Additional studies still need to verify that bioconjugates are biologically inert and that interactions other then with its cognate receptor are not occurring. Inertness can additionally be defined as the ability of the particle to circumvent the body without being removed or nonspecifically accumulating in various tissue systems. The particle must be able to travel the blood system and seek out the choice target, while minimally interacting with other locations in the body. Additionally, particle targeting and localization within a tissue or cell must be further tested and understood. It is still not understood whether the induction of apoptosis or necrosis for cell death is most effective in therapy. As such, cancer cells can be targeted in a variety of locations, ranging from various subcellular components (e.g., DNA or proteins) to the plasma membrane. Where the particle is spatially located within the cell will also affect the degree of optical localization necessary. For example, targeting a molecular macromolecule will require far greater spatial confinement than is necessary to photodamage the plasma membrane. One major hurdle that is now only being realized is bifunctionalization of particles for directionality into the cell and attachment to the desired intracellular target. To target intracellular sites, delivery methods need to still be developed. Researchers have just recently demonstrated intracellular delivery of gold nanoparticles utilizing the TAT protein from the HIV virus [119,120]. Stealth based nanoshuttles (e.g. liposomes and viruses) are also beginning to be developed for the transportation of nanoparticles to a particle region of interest [121]. Typically these vessels are biodegradable or become part of the cellular membrane upon attachment to interest target. Such nanoshuttles have the potential to deliver a large payload of nanoparticles into the target tissue or cell with high specificity.

Laser irradiation parameters are directly related to both the particle geometry and biological setting. Each particle type has a unique absorption and scattering spectrum. The laser wavelength should be chosen to maximize the interaction between the laser and the particle, so that the most effective therapy can be achieved. Particle type and laser wavelength and its

duration will be a function of the tissue type and of the tumor location. Depending upon the tissue structure, a particular particle size maybe necessary. For tissue having a large volume of connective tissue, smaller particles such as nanorods maybe necessary, which will dictate the laser wavelength. On the other hand, type of tumor whether it is solid or scattered among the healthy cells, will determine the laser pulse duration. The physical delivery of laser light is additionally of great importance. The development of probe-based technology that minimizes patient discomfort while effectively irradiating the entire region of interest is desired. The delivery mode will depend upon the location of the lesion. For lesions of the oral cavity, the use of endoscopic probes or the modification of existing dental devices will prove necessary.

Finally, working towards multimodal therapies is of great importance; it will be absolutely necessary for the combination of therapeutic and imaging techniques and for the combination of multiple therapies. Smart particles for combined imaging (MRI/Optical) and photothermal therapy [122,123] and that combine phototherapy with other therapies such as photodynamic therapy [124] are only just being realized.

In initial *in-vitro* studies, PLP has demonstrated enhanced therapeutic applications for increased efficacy in cancer treatment. In this section, we provided examples of clinical applications and discussed how the biological limits affect the optical and particle parameters. We also discussed how the physical properties of bioconjugates must further be understood to develop the next generation of smart phototherapeutic particles. As the optical and particle parameters are further refined, particle development matures, and *in-vivo* laser delivery techniques for both depth and surface applications are developed, plasmonic phototherapy has the potential to become the gold standard in various cancer treatments.

7. Acknowledgements:

We would like to thank R.K. Harrison for his help computing optical cross-sections, A. Plech for providing his experimental data, and B. Luk'yanchuk for nanoparticle scattering intensity modeling. Some of the research presented in this work was supported by the National Institutes of Health grant RO3 CA125774 and by the Texas Higher Education Coordinating Board through Advanced Research Program (ARP) grant.

8. References:

[1] American Cancer Society, Cancer Facts and Figures., 2008.

[2] U.S. Department of Health and Human Services, Cancer Nanotechnology Plan: A Strategic Initiative to Transform Clinical Oncology and Basic Research Through the Directed Application of Nanotechnology., 2004.

[3] Sokolov, K., Aaron, J., Hsu, B., Nida, D., Gillanwater, A., Follen, M., Macaulay, C., Adler-Storthz, K., Korgel, B., Discour, M., Pasqualini, R., Arap, W., Lam, W., and Richartz-Kortum, R., Optical systems for in vivo molecular imaging of cancer, Technol. Cancer Res. Treat. 2003, **2**(6), 491-504.

[4] El-Sayed, I.H., Huang, X., and El-Sayed, M.A., Surface plasmon resonance scattering and absorption of anti-EGFR antibody conjugated gold nanoparticles in cancer diagnostics: Applications in oral cancer, Nano Lett. 2005, **5**, 829-834.

[5] Huang, X, El-Sayed, I.H., Qian, W., and Els-Sayed, M.A., Cancer cell imaging and photothermal therapy in the near-infrared region by using gold nanorods, J. Am. Chem. Soc. 2006, **128**, 2115-2120.

[6] Durr, N.J., Larson, T., Smith, D.K., Korgel, B.A., Sokolov, K., and Ben-Yakar, A., Two-photon luminescence imaging of cancer cells using molecularly targeted gold nanorods, Nano Lett. 2007, **7**(4), 941-945.

[7] Bohren, C.F. and Huffman, D.R., *Absorption and Scattering of Light by Small Particles,* John Wiley & Sons, Inc., New York (1983).

[8] Pourbaix, M., Electrochemical corrosion of metallic biomaterials, Biomaterials 1984, **5**, 122-134.

[9] Lewinski, N., Colvin, V., and Drezek, R., Cytotoxicity of nanoparticles, Small 2008, **4**(1), 26-49.

[10] Turkevich, J., Stevenson, P.C., and Hillier, J., A study of the nucleation and growth processes in the synthesis of colloidal gold, Discuss Faraday Soc. 1951, **11**, 551951.

[11] Frens, G., Controlled nucleation for the regulation of the particle size in monodisperse gold suspensions, Nat. Phys. Sci. 1973, **241**, 20-22.

[12] Link, S. and El-Sayed, M.A., Spectral properties and relaxation dynamics of surface plasmon electronic oscillations in gold and silver nanodots and nanorods, J. Phys. Chem B 1999, **34**, 8410-8426.

[13] Zhou, H.S., Honma, I., and Komiyama, H., Controlled synthesis and quantum-size effects in gold-coated nanoparticles, Phys. Rev. B 1994, **50**, 12052-12056.

[14] Oldenburg, S.J., Averitt, R.D., Westcott, S.L., and Halas, N.J., Nanoengineering of optical resonances, Chem. Phys. Lett. 1998, **288**, 243-247.

[15] Chen, J., Saeki, F., Wiley, B., Cang, H., Cobb, M.J., Li, Z.-Y., Au, L., Zhang, H., Kimmey, M.B., Li, X., and Xia, Y., Gold nanocages: bioconjugation and their potential use as optical imaging contrast agents, Nano Lett. 2005, **5**, 473-477.

[16] Zharov, V., Galitovsky, V., and Viegas, M., Photothermal detection of local thermal effects during selective nanophotothermolysis, Appl. Phys. Lett. 2003, **83**, 4897-4899.

[17] Lapotko, D.O., Lukianova, E., and Oraevsky, A.A., Selective Laser Nano-Thermolysis of Human Leukemia Cells with Microbubbles Generated Around Clusters of Gold Nanoparticles., Las. Surg. Med. 2006, **38**, 631-642.

[18] Wong, N., O'Connell, M., Wisdom, J.A., and Dai, H., Carbon Nanotubes as Mulitfunctional Biological Transporters and Near-Infrared Agents for Selective Cancer Cell Destruction., PNAS 2005, 102, 11600-11605.

[19] Kim, J.W., Shashkov, E.V., Galanzha, E.I., Kotagiri, N., and Zharov, V.P., Photothermal Antimicrobial Nanotherapy and Nanodiagnostics with Self-Assembling Carbon Nanotube Clusters., Las. Surg. Med. 2007, 39, 622-634.

[20] Son, S.J., Bai, X., and Lee, S., Inorganic Hollow Nanoparticles and Nanotubes in Nanomedicine: Part 2. Imaging, Diagnostics, and Therapeutic Applications., Drug Discovery Today 2007, 12, 657-663.

[21] Shao, N., Lu, S., Wickstrom, E., and Panchapakesan, B., Integrated Molecular Targeting of IGF1R and HER2 Surface Receptors and Destruction of Breast Cancer Cells using Single Wall Carbon Nanotubes., Nanotechnology 2007, 18, 315101.

[22]Geoghegan, W.D. and Ackerman, G.A., Adsorption of horseradish peroxide, ovomucoid, and anti-immunoglobulin to colloidal gold for the indirect detection of concanavalin A, wheat germ agglutinin, goat anti-human immunoglobulin G on cell surfaces at the electron microscope level: a new method, theory, and application, J. Histochem. 1977, **25**, 1187-1200.

[23] Loo, C., Lowery, A., Halas, N.J., West, J., and Drezek, R.A., Immunotargeted Nanoshells for Integrated Cancer Imaging and Therapy., Nano Lett. 2005, **5**, 709-711.

[24] Csaki, A., Garwe, F., Steinbruck, A., Maubach, G., Festag, G., Weise, A., Riemann, I., Konig, K., and Fritzsche, W., A Parallel Approach for Subwavelength Molecular Surgery Using Gene-Specific Positioned Metal Nanoparticle as Laser Light Antennas., Nano Lett. 2007, **7**, 247-253.

[25] Huff, T.B., Tong, L., Zhao, Y., Hansen, M.N., Cheng, J., and Wei, A., Hyperthermic Effects of Gold Nanorods on Tumor Cells., Nanomedicine 2007, **2**, 125-132.

[26] Tong, L., Zhao, Y., Huff, T.B., Hansen, M.N., Wei, A., and Cheng, J., Gold Nanorods Mediate Tumor Cell Death by Compromising Membrane Integrity., Adv. Mater. 2007, **19**, 3136-3141.

[27] Niidome, T., Yamagata, M., Okamoto, Y., Akiyama, Y., Takahashi, H., Kawano, T., Katayama, Y. and Niidome, Y., PEG-modified gold nanorods with a stealth character for in vivo applications, J. Controlled Release 2006, **114**, 343-347.

[28] Chem. A.M. and Scott, M.D., Current and future applications of immunological attenuation via pegylation of cells and tissue, BioDrugs 2001, **15**, 833-847.

[29] Harris, J.M., Martin, N.E., and Modi, M., Pegylation: a novel process for modifying pharmacokinetics, Clin. Pharamacokinet. 2001, **40**, 539-551.

[30] Kumar, S. and Richards-Kortum, R., Optical molecular imaging agents for cancer diagnostics and therapeutics, Nanomedicine 2006, **1**, 23-30.

[31] Sokolov, K., Nida, D., Descour, M., Lacy, A., Levy, M., Hall, B., Dharmawardhane, S., Ellington, A., Korgel, B., and Richards-Kortum, R., Molecular optical imaging of therapeutic targets of cancer, Adv. Cancer Res. 2006, **96**, 299-344.

[32] Huang, X., Prashant, K.K., El-Sayed, I.H., and El-Sayed, M.A., Plasmonic photothermal therapy (PPTT) using gold nanoparticles, Laser Med. Sci. 2007, **23**(3), 217-228.

[33] Huang, X., Prashant, K.K., El-Sayed, I.H., and El-Sayed, M.A., Gold nanoparticles and nanorods in medicine: From cancer diagnostics to photothermal therapy, Nanomedicine 2007, **2**(5), 681-693.

[34] H.C. van de Hulst, *Light Scattering by Small Particles*. John Wiley & Sons, New York (1957)

[35] Kreibig, U. and Vollmer, M., *Optical Properties of Metal Clusters.,* Springer, Berlin (1995).

[36] Kerker, M., *The Scattering of Light and Other Electromagnetic Radiation*., Academic, New York (1969).
[37] Jackson, J.D., *Classical Electrodynamic*., John Wiley & Sons, New York, 3rd edition (1999).
[38] Papavassiliou, G.C., Optical properties of small inorganic and organic metal particles, Prog. Solid State Chem. 1979, **12**, 185.
[39] Wagner, F.E., Haslbeck, S., Stievano L., Calogero, S., Pankhurst, O.A., and Martinek, K.P., Before striking gold in gold-ruby glass, Nature 2000, **407**, 691.
[40] M. Kerker, The optics of colloidal silver: something old and something new, J. Colloid Interface Sci. 1985, **105**, 297.
[41] Yguerabide, J. and Yguerabide, E.E., Light-Scattering Submicroscopic Particles as Highly Fluorescent Analogs and Their Use as Tracer Labels in Clinical and Biological Applications I. Theory, Anal.. Biochem. 1998, **262**, 137.
[42] Kelly, R.L., Coronado, E., Zhao, L.L., and Schatz, G.C., The Optical Properties of Metal Nanoparticles: The Influence of Size, Shape, and Dielectric Environment, J. Phys. Chem. B 2003, **107**, 668.
[43] Messinger, B.J., Ulrich von Raben, K., Chang, R.K., and Barber, P.W., Local fields at the surface of noble-metal microspheres, Phys. Rev. B 1981, **24**, 649.
[44] Drude, P., Electron theory of metals- Part I, Ann. Phys. 1900, **1**, 556.
[45] Drude, P., Electron theory of metals- Part II, Ann. Phys. 1900, **3**, 369.
[46] Drude, P., Electron theory of metals- Correction, Ann. Phys. 1902, **7**, 687.
[47] Hovel, H., Fritz, S., Hilger, A., Kreibig, U., and Vollmer, M., Width of cluster plasmon resonances: Bulk dielectric functions and chemical interface damping, Phys. Rev. B 1993, **48**, 178.
[48] Bassani, F. and Parravicini, G.P., *Electronic States and Optical Transitions in Solids*. Pergamon, New York (1975)
[49] Alvarez, M.M., Khoury, J.T., Schaaff, T.G., Shafigullin, M.N., Vezmar, I., and Whetten, R.L., Optical absorption spectra of nanocrystal gold molecules, J. Phys. Chem. B 1997, **101**, 3706.
[50] Link, S. and El-Sayed, M.A., Size and temperature dependence of the plasmon absorption of colloidal gold nanoparticles, J. Phys. Chem. B 1999, **103** 4212.
[51] Ashcroft, N.W. and Mermin, N.D., *Solid state Physics*. Saunders College, Philadelphia (1976).
[52] Kuhn, H. in: Hoppe, W., Lohmann, W., Mark., H., and Ziegler, H. (Eds.), Biophysik, Springer, Berlin (1982), 289.
[53] Rechberger, W., Hohenau, A. Leitner, A., Krenn, F.R., Lamprecht, B., and Aussenegg, F.R., Optical properties of two interacting gold particles, Opt. Comm. 2003, **220** 137.
[54] Quinten, M., Local fields close to the surface of nanoparticles and aggregates of nanoparticles, Appl. Phys. B 2001, **73**, 245-255.
[55] Maier, S.A., Brongersma, M.L., Kik, P.G., and Atwater, H.A., Observation of near-field coupling in metal nanoparticle chains using far-field polarization spectroscopy, Phys. Rev. B 2002, **65**, 193408.
[56] Khlebtsov, B., Zharov, V., Melnikov, A., Tuchin, V., and Khlebtsov, N., Optical amplification of photothermal therapy with gold nanoparticles and nanoclusters, Nanotech. 2006, **17**, 5167-5179.
[57] Eversole, D.S., Plasmonic laser nanoablation of solid material, Master Thesis 2007, University of Texas at Austin.

[58] Sinzig, J. and Quinten, M., Scattering and absorption by spherical multilayer particles, Appl. Phys. A 1994, **58**, 157-162

[59] Sinzig, J., Radtke, U., Quinten, M., and Kreibig, U., Binary clusters: homogeneous alloys and nucleus-shell structures, Z. Phys. D 1993, **26**, 242-245.

[60] Chen, J., Wang,. D., Xi, J. Au, L., Siekkinen, A., Warson, A., Li, Z.-Y., Zhang, H., Xia, Y., and Li, X., Immuno gold nanocages with tailored optical properties for targeted photothermal destruction of cancer cells, Nano Lett. 2007, **7**, 1318-1322.

[61] Hirsch, L.R., Gobin, A.M., Lowery, A.R., Tam, F., Drezek, R.A., Halas, N.J., and West, J.L., Metal Nanoshells, Ann. Biomed. Eng. 2006, 34, 15-22.

[62] Mohamed, M.B., Ismael, K.Z., Link, S, and El-Sayed, M.A., J. Phys. Chem B 1998, **102**, 9370.

[63] Shankar, S.S., Rai, A., Ankamar, B., Singh, A., Ahmad, A., and Sastry, M., Biological synthesis of triangular gold nanoprisms, Nature Mat. 2004, **3**, 482.

[64] Wang, H., Brandl, D.W., Le, F., Nordlander, P., and Halas, N.J., Nanorice: a hybrid nanostructure, Nano Lett. 2006, **6**, 827.

[65] Link, S. and El-Sayed, M.A., Shape and size dependence of radiative, nonradiative, and photothermal properties of gold nanocrystals, Int. Rev. Phys. Chem. 2000, **19**, 409-453.

[66] Specht, M., Pedarnig, J.D., Heckl, W.M., and Haensch, T.W., Scanning Plasmon Near-Field Microscope, Phys. Rev. Lett. 1992, **68**, 476.

[67] Boyd, G.T., Rasing, Th., Leite, J.R.R., and Shen, Y.R., Local-field enhancement on rough surfaces of metals, semimetals, and semiconductors with the use of optical second-harmonic generation, Phys. Rev B 1984, **30**, 519.

[68] Krug, J.T. II, Sanchez, E.J., Xie, X.S., and Sunney, X., Design of near-field probes with optimal field enhancement by finite difference time domain electromagnetic simulation, J. Chem. Phys. 2002, **116** 10895.

[69] Hartland, G.V., Hu, M., and Sader, J.E., Softening of the symmetric breathing mode in gold particles by laser-induced heating, J. Phys. Chem. B 2003, 107, 7472-7478.

[70] Petrova, H., Hu, M., and Hartland, G.V., Photothermal properties of gold nanoparticles, Z. Phys. Chem. 2007, 221, 361–376.

[71] Hu, M., and Hartland, G.V., Heat dissipation for Au particles in aqueous solution: Relaxation time versus size, J. Phys. Chem. B 2002, 106, 7029-7033.

[72] Wilson, O.M., Hu, X., Cahill, D.G., and Braun, P.V., Colloidal metal nanoparticles as probes of nanoscale thermal transport in fluids, Physical Review B 2002, 66, 224301.

[73] Ge, Z., Kang, Y., Taton, T.A., Braun, P.V., and Cahill, D.G., Thermal transport in Au-core polymer-shell nanoparticles, Nano Lett. 2005, **5**, 3, #.

[74] Plech, A., Kotaidis, V., Grésillon, S., Dahmen, C., and von Plessen G., Laser-induced heating and melting of gold nanoparticles studied by time-resolved x-ray scattering, Physical Review B 2004, 70, 195423.

[75] Kaganov, M., Lifshitz, I.M. and Tanatarov, L.V., Relaxation between electrons and crystalline lattices, *Sov. Phys. JETP* 1957, **4**, 173.

[76] Ekici, O., Harrison, R.K., Durr, N.J., Eversole, D.S., Lee, M., and Ben-Yakar, A., Thermal Analysis of Gold Nanorods Heated with Femtosecond Laser Pulses, submitted to J. Phys. D: Appl. Phys. 2008, **41**(18), 185501.

[77] Kotaidis, V., Dahmen, C., von Plessen, G., Springer, F., and Plech, A., Excitation of nanoscale vapor bubbles at the surface of gold nanoparticles in water, J. Chem. Phys. 2006, 124, 184702.

[78] Willis, D.A., and Xu, X., Heat transfer and phase change during picosecond laser ablation of nickel, Int. J. Heat and Mass Trans. 2002, **45**, 3911-3918.
[79] Martynyuk, M.M., Vaporization and boiling of liquid metal in an exploding wire., Soviet Phys., Tech. Phys. 1974, **19** (6), 793–797.
[80] Xu, X., Phase explosion and its time lag in nanosecond laser ablation, *Applied Surface Science* 2002, 197-198, 61-66.
[81] Volkov, A.N., Sevilla, C., and Zhigilei, L.V., Numerical modeling of short pulse laser interaction with Au nanoparticle surrounded by water, *Applied Surface Science* 2007, **253**, 6394-6399.
[82] Dou, Y., Zhigilei, L.V., Winograd, N., and Garrison, B.J., Explosive boiling of water films adjacent to heated surfaces: A microscopic description, *J. Phys. Chem. A* 2001, **105**, 2748-2755.
[83] Hu, M., Petrova, H., and Hartland, G.V., Investigation of gold nanoparticles in aqueous solution at extremely high lattice temperatures, *Chemical Physics Letters* 2004, **391**, 220-225.
[84] Debenedetti, P.G. *Metastable Liquids: Concepts and Principles*, Princeton University Press, Princeton, 1996.
[85] Inasawa, S., Sugiyama, M., Yamaguchi, Y., Laser-induced shape transformation of gold nanoparticles below the melting point: The effect of surface melting, J. Phys. Chem. B, 2005, 109, 3104-3111.
[86] Link, S., and El-Sayed, M.A., Spectroscopic determination of the melting energy of a gold nanorod, J. Chem. Phys., 2001, 114, 2362-2368.
[87] Link, S., Burda, C., Nikoobakht, B., and El-Sayed, M.A., Laser-induced shape changes of colloidal gold nanorods using femtosecond and nanosecond laser pulses, J. Phys. Chem. B, 2000, 104, 6152-6163.
[88] Huttmann, G., Radt, B., Serbin, J., Lange, B.I., and Birngruber, R., High precision cell surgery with nanoparticles?, Med. Laser Appl. 2002, **17**, 9-14.
[89] Pitsillides, C.M., Joe, E.K., Wei, X., Anderson, R.R., and Lin, C.P., Selective cell targeting with light-absorbing microparticles and nanoparticles, Biophys. J 2003, **84**, 4023-4032.
[90] Csaki, A., Garwe, F., Steinbruck, A., Maubach, G., Festag, G., Weise, A., Riemann, I., Konig, K., and Fritzsche, W., A Parallel Approach for Subwavelength Molecular Surgery Using Gene-Specific Positioned Metal Nanoparticle as Laser Light Antennas., Nano Lett. 2007, **7**, 247-253.
[91] Mazumder, A. and Shivashankar, G.V., Gold-Nanoparticle-Assisted Laser Perturbation of Chromatin Assembly Reveals Unusual Aspects of Nuclear Architecture within Living Cells., Biophys. J. 2007, **93**, 2209-2216.
[92] Yao, C.P., Rahmanzadeh, R., Endl, E., Zhang, Z.X., Gerdes, J., and Huttmann, G.J., Elevation of plasma membrane permeability by laser irradiation of selectively bound nanoparticles., Biomed. Opt. 2005, **10**, 064012.
[93] Everts, M., Saini, V., Leddon, J.L., Kok, R.J., Stoff-Khalili, M., Preuss, M.A., Millican, C.L., Perkins, G., Brown, J.M., Bagaria, H., Nikles, D.E., Johnson, D.T., Zharov, V.P., and Curiel, D.T., Covalently Linked Au Nanoparticles to a Viral Vector: Potential for Combined Photothermal and Gene Cancer Therapy., Nano Lett. 2006, **6**, 587-591.
[94] Zharov, V.P., Mercer, K.E., Galitovskaya, E.N., and Smeltzer, M.S., Photothermal Nanotherapeutics and Nanodiagnostics for Selective Killing of Bacteria Targeted with Gold Nanoparticles., Biophys. J. 2006, **90**, 619-627.
[95] Svaasand, L.O. Gomer, C.J., and Morinelli, E., On the physical rationale of laser induced hyperthermia., Lasers Med. Sci 1990, **5**, 121-128.

[96] Lowery, A.R., Gobin, A.M., Day, E.S., Halas, N.J., and West, J.L., Immunonanoshells for Targeted Photothermal Ablation of Tumor Cells., Int. J. Nanomed. 2006, **1**, 149-154.
[97] Hirsch, L.R., Stafford, R.J., Bankson, J.A., Sershen, S.R., Rivera, B., Price, R.E., Hazle, J.D., Drezek, R.A., Halas, N.J., and West, J.L., Nanoshell-Mediated Near-Infrared Thermal Therapy of Tumors under Magnetic Resonance Guidance., PNAS 2003, **100**, 13549-13554.
[98] Stern, J.M., Stanfield, J., Lotan, Y., Park, S., Hsieh, J.T., and Cadeddu, J.A., Efficacy of Laser-Activated Gold Nanoshells in Ablating Prostate Cancer Cells in Vitro., J. Endourology 2007, **21**, 939-943.
[99] El-Sayed, I.H., Huang, X.H., and El-Sayed, M.A., Selective Laser Photo-Thermal Therapy of Epithelial Carcinoma using anti-EGFR Antibody Conjugated Gold., Cancer Lett. 2006, **239**, 129-135.
[100] Huang, X.H., Jain, P.K., El-Sayed, I.H., and El-Sayed, M.A., Determination of the Minimum Temperature Required for Selective Photothermal Destruction of Cancer Cells with the Use of Immunotargeted Gold Nanoparticles., Photochem. & Photobio. 2006, **82**, 412-417.
[101] Gobin, A.M., Lee, M.H., Halas, N.J., James, M.D., and Drezek, R.A., Near-Infrared Resonant Nanoshells for Combined Optical Imaging and Photothermal Cancer Therapy., Nano Lett. 2007, **7**, 1929-1934.
[102] Anderson, R.R. and Parrish, J.A., Selective photothermolysis: precise microsurgery by selective absorption of pulsed radiation., Science 1983, **220**, 524-527.
[103] Lin, C.P., Kelly, M.W., Sibayan, S.A.B., Latina, M.A., and Anderson, R.R., Selective cell killing by microparticle absorption of pulsed laser radiation., IEEE J. Sel. Top. Quant. Elect. 1999, **5**, 963-968.
[104] Huttmann, G. and Birngruber, R., On the Possibility of High-Precision Photothermal Microeffects and the Measurement of Fast Thermal Denaturation of Proteins., IEEE J. Sel. Top. Quant. Elect. 1999, **5**, 954-962.
[105] Goldenberg, H. and Tranter, C.J., Heat flow in an infinite medium heated by a sphere., Brit. J. Appl. Phys. 1952, **3**, 296-298.
[106] Takahashi, H.., Niidome, Y., and Yamada, S., Gold Nanorod-sensitized Cell Death: Microscopic Observation of Single Living Cells Irradiated by Pulsed Near-Infrared Laser Light in the Presence of Gold Nanorods., Chem. Lett. 2006, 35, 500-501.
[107] Takahashi, H., Niidome, T., Nariai, A., Niidome, Y., and Yamada, S., Photothermal Reshaping of Gold Nanorods Prevents Further Cell Death, Nanotech. 2006, 17, 4431-4435.
[108] Letfullin, R.R., Joenathan., C., George, T.F., and Zharov, V.P., Laser-Induced Explosion of Gold Nanoparticles: Potential Role for Nanophotothermolysis of Cancer., Nanomedicine 2006, **1**, 473-480.
[109] Vrouenraets, M.B., Visser, G.W.M., Stigter, M., Oppelaar, H., Snow, G.B., and van Dongen, G.A.M.S., Targeting of aluminum (III) phthalocyanine tetrasulfonate by use of internalized monoclonal antibodies: improved efficacy in photodynamic therapy., Cancer Res. 2001, **61**, 1970-1975.
[110] Miller, K., Beardmore, J., Kanety, H., Schlessinger, J., and Hopkins, C.R., Localization of the epidermal growth factor (EGF) receptor within the endosome of EGF-stimulated epidermoid carcinoma (A431) cells., J. Cell Bio. 1986, **102**, 500-509.
[111] Zharov, V.P., Letfullin, R.R., and Galitovskaya, E.N., Microbubbles-overlapping mode for laser killing of cancer cells with absorbing nanoparticle clusters., J. Physics D Appl. Phys. 2005, 38, 2571-2581.

[112] Zharov, V.P., Galitovskaya, E.N., Johnson, C., and Kelly, T., Synergistic Enhancement of Selective Nanophotothermolysis with Gold Nanoclusters: Potential for Cancer Therapy., Las. Surg. Med. 2005, 37, 219-226.
[113] Larson, T.A., Bankson, J., Aaron, J., and Sokolov, K., Hybrid plasmonic magnetic nanoparticles as molecular specific agents for MRI/optical imaging and phototherma, therapy of cancer cells., Nanotechnology 2007, 18, 325101.
[114] Tirlapur, U.K., and König, K., Cell biology: targeted transfection by femtosecond laser., Nature 2002, 418, pp. 290–291.
[115] Yanik, M.F., Cinar, H., Cinar, H.N., Chisholm, A.D., Jin, Y., and Ben-Yakar, A., Functional regeneration after nanoaxotomy., Nature 2004, 432, 882.
[116] Shen, N., Datta, D., Schaffer, C.B., LeDuc, P., Ingber, D.E., and Mazur, E., Ablation of cytoskeletal filaments and mitochondria in cells using a femtosecond laser nanoscissor., Mech. Chem Biosys. 2005, **2**, 17-26.
[117] Vogel, A, Noack, J, Hüttmann, G, and Paltauf, G: Mechanisms of femtosecond laser nanosurgery of cells and tissues., Appl. Phys. B 2005, 81, 1015-1047.
[118] Eversole, D., Luk'yanchuk, B., and Ben-Yakar, A., Plasmonic laser nanoablation of silicon by the scattering of femtosecond pulses near gold nanospheres., Appl. Phys. A 2007, invited paper, 89, 283-291.
[119] Kumar, S., Harrison, N., Richards-Kortum, R., and Sokolov, K., Plasmonic nanosensors for imaging intracellular biomarkers in live cells., Nano Lett. 2007, 7, 1338-1343.
[120] Kumar, S., Aaron, J., and Sokolov, K., Directional conjugation of antibodies to nanoparticles for synthesis of multiplexed optical contrast agents for both delivery and targeting moieties., Nat. Prot. 2008, 3, 314-320.
[121] Choi, M.R., Stanton-Maxey, K.J., Stanly, J.K., Levin, C.S., Bardhan, R., Akin, D., Badve, S., Sturgis, J., Robinson, J.P., Bashir, R., Halas, N.J., Clare, S.E., A Cellular Trojan Horse for Delivery of Therapeutic Nanoparticles into Tumors, Nano Lett. 2007, 7, 3759-3765.
[122] Ji, X.J., Shao, R.P., Elliot, A.M., Stafford, R.J., Esparza-Cross, E., Bankson, J.A., Liang, G., Luo, Z.P., Park, K., Markert, J.T., and Li, C., Bifunctional Gold Nanoshells with a Supermagnetic Iron Oxide-Silica Suitable for Both MR Imaging and Photothermal Therapy., J. Phys. Chem C 2007, 111, 6245-6251.
[123] Kim, J., Park, S., Lee, J.E., Jin, S.M., Lee, J.H., Lee, I.S., Yang, I., Kim, J.S., Kim, S.K., Cho, M.H., and Hyeon, T., Designed Fabrication of Multifunctional Magnetic Gold Nanoshells and their Application to Magnetic Resonance Imaging and Photothermal Therapy., Angewandte Chemie-International Edition 2006, 45, 7754-7758.
[124] Weider, M.E., Hone, D.C., Cook, M.J., Handsley, M.M., Gavrilovic, J., and Russel, D.A., Intracellular Photodynamic Therapy with Photosensitizer-Nanoparticle Conjugates: Cancer Therapy using a 'Trojan Horse'., Photochem. & Photobio. Sci. 2006, 5, 727-734.